A dynamic *in vitro* model of Down Syndrome neurogenesis with Trisomy 21 gene dosage correction

Prakhar Bansal [1,2,†], Erin. C Banda [2,†], Heather R. Glatt-Deeley [2], Christopher E. Stoddard [3], Jeremy W. Linsley [4,5], Neha Arora [4,5,6], Darcy T. Ahern [1,2,7], Yuvabharath Kondaveeti [2,8], Michael Nicouleau [2,9], Miguel Sabariego-Navarro [10], Mara Dierssen [10,11,12,13], Steven Finkbeiner [4,5,14,15], and Stefan F. Pinter [1,2,16, *]

30 [1] Graduate Program in Genetics and Developmental Biology, UCONN Health, University of
31 Connecticut, Farmington, CT, United States
32 [2] Department of Genetics and Genome Sciences, UCONN Health, University of Connecticut,
33 Farmington, CT, United States
34 [3] Cell and Genome Engineering Core, UCONN Health, University of Connecticut, Farmington, CT,
35 United States
36 [4] Center for Systems and Therapeutics, Gladstone Institutes, San Francisco, United States
37 [5] Taube/Koret Center for Neurodegenerative Disease, Gladstone Institutes, San Francisco, CA
38 [6] Current: Department of Biology, Brandeis University, Waltham, MA, United States
39 [7] Current: Intellia Therapeutics, Cambridge, MA, United States
40 [8] Current: Enzerna Biosciences, Morrisville, NC, United States
41 [9] Current: Early Drug Discovery Unit, Montreal Neurology Institute, McGill University
42 [10] Centre for Genomic Regulation (CRG), The Barcelona Institute of Science and Technology,
43 08003 Barcelona, Spain
44 [11] Universitat Pompeu Fabra (UPF), Barcelona, Spain.
45 [12] Human Pharmacology and Clinical Neurosciences Research Group, Neurosciences Research
46 Program, Hospital Del Mar Medical Research Institute (IMIM), 08003 Barcelona, Spain
47 [13] Centro de Investigación Biomédica en Red de Enfermedades Raras (CIBERER), Spain
48 [14] Departments of Neurology and Physiology, University of California San Francisco, San
49 Francisco, CA, United States
50 [15] Neuroscience and Biomedical Sciences Graduate Programs, University of California San
51 Francisco, San Francisco, United States
52 [16] Institute for Systems Genomics, University of Connecticut, Farmington, CT, United States
53
54
55 † These authors contributed equally
56 * Corresponding author: spinter@uchc.edu
57
58

ABSTRACT/SUMMARY

Excess gene dosage from human chromosome 21 (chr21) causes Down syndrome (DS), spanning developmental as well as acute phenotypes in terminal cell types. Which phenotypes remain amenable to intervention after development is unknown. To address this question in a model of DS neurogenesis, we generated trisomy 21 (T21) human induced pluripotent stem cells (hiPSCs) alongside otherwise isogenic euploid controls from mosaic DS fibroblasts, and integrated an inducible *XIST* transgene on one chr21 copy. Monoallelic chr21 silencing by *XIST* was near-complete and irreversible in hiPSCs. Differential expression reveals T21 neural lineages and T21 hiPSCs suppress similar translation and mitochondrial pathways, and activate cellular stress responses. When *XIST* is induced before the neural progenitor stage, T21 dosage correction mitigates a pronounced skew towards astrogenesis in differentiation. Because our transgene remained inducible in post-mitotic T21 neurons and astrocytes, we demonstrate *XIST* efficiently represses genes even after terminal differentiation, which will empower exploration of cell type-specific T21 phenotypes that remain responsive to chr21 dosage.

88 **INTRODUCTION**

89 As the most prevalent human viable aneuploidy (trisomy 21, T21 in up to 1:800-1:1000 live
90 births), Down syndrome (DS) poses three significant challenges to understanding and addressing
91 the clinical needs of people living with DS [1]. First, our understanding of the developmental
92 etiology underlying cardiac, hematopoietic and neurological defects in DS is still limited [2]. Ever-
93 more sophisticated rodent DS models faithfully carry most of human chromosome 21 (chr21) [3,4]
94 or traverse syntenic boundaries to represent supernumerary mouse chr21 orthologs [5]. While
95 these rodent models capture many important aspects of DS, human T21 induced pluripotent
96 stem cells (hiPSCs) are serving as an important complementary model for DS development and
97 pre-clinical research [6]. These hiPSC models may prove especially relevant to human-specific
98 aspects of development, for example by reflecting brain region-specific neural cell types [7],
99 intrinsically longer human neuronal maturation [8], and a more rapidly evolving susceptibility to
100 neurodegeneration that may be rooted in human neurodevelopment [9,10].

101 Second, we lack experimental approaches to systematically distinguish irreversible
102 developmental phenotypes from "acute" cellular phenotypes that may remain amenable to
103 postnatal intervention. Supernumerary chr21 genes, or their rodent orthologs, are present
104 throughout differentiation or development of such DS hiPSC and rodent DS models, respectively.
105 With few exceptions [11], we therefore have an incomplete view of which T21 phenotypes depend
106 on ongoing excess dosage of specific chr21 genes in terminally differentiated cells. This question
107 is particularly relevant to DS-associated neurodegeneration [12].

108 Third, cellular stress pathways that are chronically and systemically active in DS [13–18] and likely
109 play an important role in DS neurodegeneration [19], are also shared with human trisomies 13 (T13)
110 and 18 (T18) [20], but not with dosage-compensated sex-chromosomal trisomy. The most plausible
111 origin for such common aneuploidy-associated cellular stress is the cumulative excess expression
112 of the many autosomal genes that code for subunits of dosage-sensitive protein complexes.
113 However, this interpretation has not yet been tested formally in the context of an autosomal
114 trisomy, as it requires distinguishing excess expression from the mere presence of the
115 supernumerary chromosome.

116 A human cellular model with dynamic T21 gene dosage would be instrumental towards
117 addressing these challenges, across a range of DS-affected cell fates and phenotypes. To
118 characterize the impact of T21 in hiPSCs and terminally differentiated cell types, we generated
119 our own dynamic hiPSC model of T21 dosage alongside otherwise isogenic controls from mosaic
120 DS. Pioneering work by the Lawrence lab demonstrated the utility of the long non-coding RNA
121 *XIST*, which endogenously silences the inactive X in females, for T21 dosage correction in DS
122 hiPSCs [21]. *XIST* RNA spreads from its site of transcription across the entire chromosome *in cis*, to
123 directly and indirectly recruit orthogonal repressive chromatin complexes to silence genes [22]. Yet,
124 earlier work in the mouse system indicated that *Xist* could establish gene silencing only during or
125 upon exiting pluripotency, but not after differentiation [23,24], with rare exception [25,26]. Recent work
126 by the Lawrence lab shows that human *XIST* can still silence genes up to the neural progenitor
127 cell (NPC) stage, but technical limitations hindered *XIST* induction in terminal, post-mitotic human
128 neural cells [27].
129 Here, we leverage phased allelic expression analysis to demonstrate that our new inducible
130 T21-*XIST* design enables uniform, near-complete and -irreversible T21 dosage correction in
131 hiPSCs. *XIST* suppresses T21 *trans*-effects, including cellular stress pathways that are also active
132 in T21 neural lineages. T21 silencing prior to the NPC stage rescues T21-altered neuro-astroglial
133 lineage balance that reflects excess gliogenesis previously observed in DS fetal samples [28–32] and
134 rodent models [33–35]. Because our T21-*XIST* system is also the first to effectively induce *XIST* and
135 repress chr21 dosage in post-mitotic neurons and astrocytes, this new model of dynamic T21
136 gene dosage will facilitate identification of cellular pathways and cell types that may present
137 promising targets for intervention after completed development.
138
139 **RESULTS**
140 **T21 dosage correction by *XIST*-mediated monoallelic silencing in DS hiPSCs**
141 To derive T21 hiPSCs alongside isogenic euploid control lines, we reprogrammed dermal
142 fibroblasts from a male individual with mosaic DS [36], and screened the resulting hiPSC clones
143 using copy-number sensitive qPCR [Fig. S1A,B]. Two T21 lines appeared to have a gain on chr17,
144 a frequent karyotypic abnormality primarily observed in human ESCs [37,38], but featured only two

145 centromere 17 signals by fluorescent *in-situ* hybridization (FISH) follow-up [Fig. S1C]. We
146 performed array comparative genomic hybridization (aCGH, CytoSNP-850k) to confirm expected
147 karyotypes for fibroblasts, euploid and T21 hiPSCs, and to resolve segmental (17q) gains in the
148 two corresponding clones, which were excluded thereafter [Fig. S1D]. Differential probe intensity
149 analysis of the remaining T21 and euploid hiPSC lines also revealed a large set of heterozygous
150 SNPs with increased representation in the euploid lines spanning chr21, and a smaller focal set
151 that was lost in euploid lines [Fig. S1E]. These results suggested one chr21 copy from each parent
152 is maintained in euploid lines ($chr21^{M}$ & $chr21^{P}$), whereas T21 hiPSCs carry an additional copy
153 ($chr21^{M2}$), likely a maternal chromatid retained via non-disjunction in meiosis II [39].
154 While T21 is stably maintained in hiPSCs after reprogramming [40–42], sporadic T21 loss has
155 been reported [43,44]. We therefore confirmed the mitotic stability of three chr21 copies by two
156 independent approaches. First, three independent signals were observed in 94.5% of T21 hiPSCs
157 by fluorescent *in-situ* hybridization (FISH, *DSCR8* probe), compared to 99% of euploid hiPSCs with
158 two signals [Fig. S1F]. Second, while targeting a *UBC*-promoter driven doxycycline (dox)-
159 responsive trans-activator (rTTA3G) to the AAVS1 safe harbor in *PPP1R12C* (HSA19), we
160 confirmed that all 32/32 independent colonies arising from single cells maintained T21 by copy-
161 number sensitive qPCR for a *DYRK1A* amplicon [Fig. S1G].
162 We integrated our TET3G-driven *XIST* cDNA transgene on $chr21^{P}$ [Fig. 1A], after re-
163 verifying the karyotypic integrity of rTTA3G clones by aCGH [Fig. S1D]. To this end, we designed
164 Cas9 guides dependent on a $chr21^{P}$-specific protospacer adjacent motif (PAM), targeting an
165 intergenic site well outside of *DYRK1A* to avoid impacting its expression. We proceeded with
166 three independent, PCR-screened T21-*XIST* clones, and tested for *XIST* induction by RNA-FISH,
167 and immuno-fluorescence (IF) staining for ubiquitinated histone 2A lysine 119 (H2AK119ub) and
168 tri-methylated histone 3 lysine 27 (H3K27me3), which follow *XIST/Xist* RNA expression on mouse
169 and human X alike [22]. Of note, because the original fibroblasts were from a male individual with
170 DS [Fig. S1C], there was no endogenous *XIST* expression, and any *XIST*/H2A119ub/H3K27me3
171 cloud must arise from the T21-targeted *XIST* transgene on chr21. Indeed, after cessation of acute
172 dox treatment (3 wk withdrawal, w/d) hiPSCs were negative for *XIST*, underscoring the TET3G
173 system is not leaky and turns off when dox is withdrawn, whereas virtually all T21-*XIST* hiPSCs

174 displayed *XIST* clouds and acquired H2A119ub/H3K27me3 signals in the presence of dox [Fig. 1B].
175 Together, these data illustrate the homogeneity of *XIST* induction, and provide independent
176 confirmation that this third copy of chr21 is faithfully maintained in hiPSCs.

177 We next performed mRNA-seq of euploid, T21 and T21-XIST hiPSCs to confirm high
178 uniformity in pluripotency genes over lineage-specific markers [Fig. S2A], and to quantify T21
179 dosage correction by *XIST* in the presence, absence or upon withdrawal of dox [Fig. 1A,C], which
180 tests whether gene silencing is maintained once established. *XIST* was uniformly expressed in all
181 three T21-XIST clones at 3, 6 and 9 weeks (wks) of dox treatment ("+dox"), and returned to the
182 ("—dox") baseline upon dox withdrawal ["w/d", Fig. 1A,C], consistent with *XIST*-negative FISH in
183 w/d samples [Fig. 1B].

184 To accurately measure chr21 dosage not only by standard differential expression analysis
185 but also chr21 allelic representation, we additionally sequenced euploid and T21 whole genomes
186 with linked-reads to identify and phase variants. In both euploid and T21 hiPSCs, most variants
187 can be grouped in large phase blocks (N50 lengths of 1.8 Mb and 2.9 Mb, respectively), including
188 across chr21, where thousands of heterozygous variants distinguish the *XIST*-bearing ($chr21^{P}$)
189 copy. Allele-specific phasing of mRNA-seq reads indeed reveals that one allele was under-
190 represented with a mean lesser allele frequency (LAF) of one-third for T21 samples. This is in
191 keeping with the presence of a single $chr21^{P}$ copy, and two copies of $chr21^{M/M2}$, whereas the
192 same $chr21^{P}$ allele comprised about half of all allelic reads in the D21 samples [Fig. 2A]. In the
193 absence of dox (-dox), the *XIST*-bearing $chr21^{P}$ copy (T21-XIST) still represented ~one-third of
194 variant-mapping reads, but was largely depleted in the +dox and w/d samples, which were dox-
195 treated (3wks) and collected after another 3 or 6 wks without dox. These data demonstrate that
196 *XIST* silences most genes on the $chr21^{P}$ copy near-completely, and irreversibly, consistent with
197 our expectations based on mouse *Xist* reports (reviewed in [22]).

198 Likewise, differential expression analysis across chr21 reveals that nearly all genes with
199 assessable expression were depleted by ~one-third (log2FC of -0.59 ± 0.15), irrespective of their
200 linear distance from the *XIST* transgene, and maintained that expression level even after 3-6 wks
201 of dox withdrawal [Fig. 2B-D]. Altogether, only a very small group of protein-coding genes
202 retained a LAF > $1/6^{th}$ (*ADAMTS1, APP, H0Y3Z8, IFNAR1/2, MRPS6, ETS2* and *YBEY*), most likely

203 due to mis-phased variants. Indeed, these genes were significantly downregulated by the
204 expected degree ($p \leq 0.1$, log2FC -0.59 ± 0.15), except for *IFNAR2* and the adjacent ORF *H0Y3Z8,*
205 which appeared to escape *XIST*-mediated repression by differential expression (p.adj > 0.1,
206 log2FC > -0.3). To compare this efficacy to previously reported T21-*XIST* systems [21,27], we
207 considered the degree of silencing across all mutually assessed chr21 genes in prior reports,
208 irrespective of adjusted p-value cutoff, as our study included a greater number of samples.
209 Indeed, the distribution log2FC values in our T21-*XIST* indicates more complete gene repression
210 than in previously published datasets [Fig. S2B].

211 Comparing differential expression in hiPSCs after 3 wk and 6wk of dox withdrawal, we
212 find that silencing was maintained in w/d samples, irrespective of the length of original dox
213 treatment [Fig. 2B, Fig. S2C]. We therefore assessed DNA methylation (DNAme) at promoters,
214 which reflects stable gene silencing known to remain intact even upon *Xist* deletion in mouse
215 fibroblasts [45,46]. Excluding likely inactive promoters with high DNAme (>60% methylated),
216 virtually all chr21 promoter-associated CpG probes of the methylEPIC array (Illumina) increased
217 from a median of 7% methylated in the absence of dox (-dox) to 41% methylated after ≥3 wks in
218 +dox [Fig. 2F]. This level is consistent with the presence of a fully methylated alongside two
219 unmethylated alleles (1/3) and is maintained ≥3 wks after dox withdrawal (w/d, 39% methylated),
220 which is also reflected in the absence of reactivated genes by differential and allelic expression
221 [Fig. 2A-E].

222 We next turned to transcriptome-wide effects of T21 and *XIST*-corrected gene dosage.
223 While levels of chr21 genes clearly increased in T21 relative to D21 and decreased in T21-XIST
224 +dox relative to -dox samples, all other chromosomes also responded to chr21 dosage, but
225 roughly balanced up- and down-regulated genes [Fig. 3A]. Consistently, samples with an effective
226 chr21 dosage matching euploid samples (D21, and +dox or w/d T21-XIST) segregated from T21
227 and no-dox T21-XIST samples in PCA [Fig. 3B]. Because our experimental design included the
228 original, non-transgenic D21 and T21 hiPSCs (198-1/2/5) with all treatments (±dox and w/d), we
229 were able to observe that their acute +dox treatment triggered expression changes that
230 correlated to some extent with the T21 dosage effect [Fig. 3C left], which was still significant after
231 excluding chr21 genes from the correlation [Fig. S3A, left]. This was not unexpected, because

232 doxycycline can partially impact mitochondrial translation in eukaryotic cells [47], and
233 mitochondrial pathways are also altered in DS [48–50]. We therefore adjusted for this small dox-
234 specific effect in our analysis (see methods). We then compared T21 over D21 log2FC expression
235 changes with the combined (+dox and w/d) *XIST* correction, which revealed a highly significant
236 and negative Pearson correlation of -0.5 [Fig. 3C, right] that persists even when chr21 genes are
237 excluded [Fig. S3A, right]. These data indicate that differentially expressed genes (DEGs)
238 responding to excess chr21 dosage are also changing in the opposite direction when excess chr21
239 dosage is corrected via *XIST*. This large-scale reversal was also evident in gene-set enrichment
240 analysis (GSEA), with a dominance of anti-correlated terms [Fig. 3D, top left and bottom right
241 quadrant], many of which related to apoptosis, stress, ER, mitochondria and translation terms.
242 Plotting the top three most-concordant terms for each of these categories [Fig. 3E], T21 and
243 dosage-corrected samples were near-uniformly opposed in biological processes previously
244 implicated in DS, including apoptosis [17,51,52], oxidative stress via NRF2 [16,53], mitochondria [18,48–50],
245 and translation [14,54]. Importantly, serine biosynthesis pathways, recently attributed to a general
246 response to aneuploidy [20] were also highly represented, indicating that serine metabolism
247 returns to baseline upon T21 dosage correction, despite the continued presence of the
248 supernumerary chr21 copy.
249
250 **T21 gene dosage effects in mature neural cell types**
251 To assess T21 gene dosage effects in neural lineages, we applied a well-established
252 monolayer differentiation protocol that mimics *in vivo* neural development in the establishment
253 of neurogenic niches (rosettes) and in the production of both mature neurons and astrocytes
254 [55,56]. We chose this approach as nearly all T21 hiPSC-derived neuronal RNA-seq data reported to-
255 date was generated from immature neurons in the absence of astrocytes. We performed mRNA-
256 seq in 10-12 wk neural cultures, obtained 5-6 wks after low-density re-plating of 4 wk NPCs [Fig.
257 S3B]. T21 neural cultures showed elevated chr21 transcript levels with a peak near the expected
258 +0.59 log2FC relative to euploid samples [Fig. 4A,B]. As expected, neural and hiPSC DEGs and
259 GSEA-enriched terms were positively correlated, while neural GSEA terms were largely anti-
260 correlated in direction with terms enriched in XIST-corrected hiPSCs [Fig. 4C-E], which also

261 extended to the three most-concordant terms across all comparisons [Fig. S3B]. Overall, we find
262 *XIST*-mediated T21 dosage correction is reflected in a majority of significantly enriched terms
263 differentiating T21 hiPSCs and neural cultures from their euploid controls [Fig. S4].
264 To assess whether the number of over-represented GSEA terms relating to cell death and
265 apoptosis in T21 neural cultures manifested in differential neuronal survival, we employed a
266 recently developed red genetically-encoded cell death indicator (RGEDI) and tracked two
267 neuronal subtypes by automated longitudinal imaging [Fig. 5A, Fig. S5A-D] [57,58]. Both T21
268 interneurons (hazard ratio of 4.08) and T21 forebrain neurons (hazard ratio of 2.57)
269 demonstrated significantly increased cell death (RGEDI/EGFP ratio > 0.15, Holm-corrected
270 $p<0.01$, linear mixed model) over ~10 days of single-cell tracking, compared to euploid controls
271 [Fig. 5B,C]. Additionally, we also assessed live neurons (RGEDI/EGFP ratio < 0.15) and noted that
272 there was a significant ($p \leq 10^{-8}$) reduction in EGFP signal in T21 compared to euploid controls [Fig.
273 S5E], that mirrored the down-regulation of ribosome and translation-related GSEA terms in both
274 T21 hiPSCs and neural cultures [Fig. 4D, Fig. S4].
275
276 **T21 dosage correction early in neural differentiation rescues neurogenesis**
277 Staining for neuronal MAP2 and astroglial S100B markers, we observed an excess of
278 astrocytes in the T21 relative to euploid neural differentiations. Both neurons and astrocytes
279 derive from NPCs [59], and astrogliosis has been reported in DS models [33,34] and fetal samples [28,30,32],
280 where T21 NPCs prematurely shift from neurogenesis to astrogenesis. To determine whether
281 *XIST*-mediated T21-dosage correction could prevent this lineage skew, we first confirmed that
282 *XIST* expression and H2AK119ub enrichment would persist in 4 wk NPCs, which was the case for
283 well over 75% of NPCs derived across three independent clones, treated with +dox as hiPSCs [Fig.
284 6A]. Indeed, even NPCs derived from untreated T21-*XIST* hiPSCs but receiving dox from the first
285 day of differentiation ("d0") presented with *XIST* and H2AK119ub foci in ≥75% and ≥65% of all
286 cells, respectively. Co-staining for MAP2 and S100B on day28 (4 wk) of neural differentiation
287 revealed a consistent and highly reproducible astrogenic skew in T21 and no-dox T21-XIST
288 samples relative to isogenic euploid control lines across multiple rounds of differentiation [Fig.
289 6B]. Remarkably, neurogenesis was fully rescued in neural differentiations from pre-treated as

290 well as d0+dox treated hiPSCs, across all three independent T21-XIST clones. Because the overall
291 sum of committed cells expressing either marker did not differ significantly between T21 and
292 euploid or T21-XIST dosage-corrected samples, we propose that T21 dosage does not suppress
293 NPC commitment in general (as suggested [27]), but rather advances the shift to astrogenesis,
294 which is consistent with reports in fetal DS and rodent DS models [30,34].
295 To test whether this interpretation is replicated *in vivo,* at the very onset of cortical
296 astrogenesis, we turned to the Ts65Dn model [Fig. S6]. At embryonic day 18.5 (E18.5), the density
297 of S100B+ positive astrocytes in the developing cortex was significantly elevated in Ts65Dn
298 embryos over their wildtype litter mates ($p < 0.05$). In contrast, there was no significant
299 difference in the density of cycling Ki67^{+} cells in the proliferative zone [Fig. S6], indicating the
300 early cortical astrogenesis in Ts65Dn embryos was not associated with delayed commitment and
301 continued proliferation of neural progenitors, but rather an inherent skew towards astrogenesis
302 also observed in other brain regions [30,34].
303
304 **Postmitotic neural cell types still induce *XIST* and attract repressive chromatin marks**
305 Given the high rate of *XIST* induction in T21-XIST NPCs that only received dox at the onset
306 of differentiation (d0), we next explored whether the *XIST* transgene would remain dox-
307 responsive in terminally differentiated cells [Fig. 7A]. To this end, we forced NPCs (~4 wk neural
308 differentiation) out of the cell cycle into terminal differentiation by inhibiting the Notch signaling
309 pathway for 5 days with gamma-secretase inhibitor DAPT, and added dox a day after completing
310 DAPT treatment (d33). To confirm DAPT treatment was sufficient to deplete mitotic cells, we also
311 labeled cells transiting S-phase with nucleotide analog EdU, and co-stained for this label and *XIST*
312 FISH after two days in +dox media (d35). DAPT-treated NPCs incorporating EdU comprised ≤6%
313 of the neural population on average, which were rarely EdU/*XIST* double-positive (≤26%),
314 whereas *XIST* was induced in ≥40% of all EdU^{-} cells (94% of all cells). We conclude that *XIST* was
315 reliably induced in a sizeable fraction of post-mitotic T21-XIST cells that had terminally
316 differentiated without dox. We next assessed these post-mitotic cells after 3 to 6 weeks of dox
317 treatment post-DAPT exposure ("pD") to provide sufficient time for H2AK119ub enrichment. We
318 included "d0" controls that were treated with the standard 1 µM dox concentration throughout

319 neural diff, as well as low-dose dox "LD" samples, which were treated with 0.01 µM dox up to
320 the DAPT exposure, and standard 1 µM dox thereafter, to test whether "pre-marking" the TRE3G
321 promoter without effective induction through differentiation may render it more responsive in
322 terminal cell types. On average, over half of d0 and LD cells featured prominent XIST clouds,
323 followed by ≥ 40% of pD samples, across both c1 and c7 clones and in three independent rounds
324 of differentiation. As before, H2AK119ub signal lagged slightly behind *XIST*, but consistently
325 marked 27% - 36% of all cells (58-65% of *XIST+* cells), including MAP2+ neurons and S100B+
326 astrocytes [Fig. 7C,D].
327
328 ***XIST* induction in terminal neurons and astrocytes corrects T21 gene dosage**
329 We next performed single-nuclei RNA-seq, to determine whether such *XIST* induction and
330 H2AK119ub accumulation in these terminally differentiated neural cell types reflect T21 dosage
331 correction [Fig. 8]. Transgenic neural differentiations treated with dox from d0 or pD were
332 collected alongside untreated T21-XIST c7 cells ("T21"), and two euploid lines (198-1/2 or
333 "D21a/b"). Nuclei distributed across four broad clusters, of which three corresponded to the
334 expected NPC, neuronal and astroglial populations [Fig. 8A, S7A]. Cell cycle analysis classified the
335 smaller NPC cluster as S and G2/M phase cells, while all other clusters scored as G1, consistent
336 with terminally differentiated G0 cells [Fig. 8A, S7A]. We labeled the first three clusters according
337 to their predominant cell type using cell type markers from [60], and the fourth as "Other" given
338 lower scores returned by sctype [61]. Due to its proximity to higher-scoring oligodendroglial
339 progenitor cells (OPC), this fourth cluster probably reflects OPC-derived lineages that
340 predominantly arose from one of the euploid lines (D21a). Crucially, *XIST* induction in T21-XIST
341 neural differentiations (d0 & pD) was detected in all clusters with 74-94% of d0+dox treated and
342 24-58% pD+dox treated cells [Fig. S7A], in agreement with our FISH and IF data [Fig. 7].
343 To determine whether *XIST* induction repressed T21 gene dosage, we assessed three
344 complementary metrics. First, we phased single-nuclei RNA-seq reads and summed allele-specific
345 counts across all chr21 genes to calculate the cumulative paternal allele representation, thereby
346 mitigating the effect of transcriptional bursts in individual nuclei [Fig. 8B]. As expected, euploid
347 cells have a significantly higher chr21^{P} allele fraction compared to T21 cells (0.46 vs. 0.32,

348 Wilcoxon p = $1.6x10^{-11}$), whereas T21-XIST day0+dox treated cells have a significantly lower
349 chr21^{P} allele fraction (0.14, Wilcoxon p < $2.2x10^{-16}$). Crucially, while *XIST*-negative pD (pD-X^{-}) cells
350 show little reduction in this *XIST*-carrying paternal allele, *XIST*-positive pD cells (pD-X^{+}) reveal
351 significant repression of this allele (0.19, Wilcoxon p-value = $1.3x10^{-12}$). Separating cells by cell
352 type group [Fig. S7B] reveals *XIST+* d0 and pD neurons repress the transgene-bearing chr21^{P} copy
353 most robustly, with paternal allele fractions of 0.15 and 0.17 (Wilcoxon p<10^{-4}), respectively.
354 Second, we compared the normalized expression for each gene on chr21 to the genome-
355 wide mean without chr21. We then determined the per-cell cumulative distribution of all chr21
356 genes, as well as the per-gene cumulative distribution by cell type group [Fig. S7C, D], and
357 aggregated these ratios across all neurons, astrocytes, and NPCs [Fig. 8C,D]. Indeed, euploid and
358 T21-nodox medians fell near the expected 1.0x and 1.5x ratios relative to the genome-wide
359 mean, indicating chr21 genes are not inherently dosage-compensated. Likewise, *XIST*-negative
360 pD nuclei failed to differ significantly from the T21-nodox sample (1.5x and 1.3x for the per-cell
361 and per-gene ratio, respectively). *XIST*+ pD nuclei however displayed near-euploid chr21 dosage
362 medians (ratios of 1.1x and 1.0x, Wilcoxon p-values ≤ $2.4x10^{-7}$), very close to d0 nuclei [Fig. 8C,D].
363 Separated by cell type group, neurons again demonstrated near-complete dosage compensation
364 in *XIST+* pD nuclei with median ratios of 0.97x and 0.92x on a per-cell and per-gene basis,
365 respectively [Fig. 8C,D]. Assessing both metrics across full distributions for each sample, the *XIST*-
366 negative pD distribution tracked closely with T21-nodox cells, remaining well within its 95%
367 confidence interval. In contrast, the *XIST+* pD and d0 distributions shifted to the left significantly
368 (dashed lines, Kolmogorov-Smirnov, K.S. test p-values) towards the euploid distributions for all
369 cell type groups, irrespective whether normalized expression ratios were averaged over cells or
370 genes [Fig. S7C, D]. Aggregating these distributions across astrocytes, neurons and NPCs
371 illustrates *XIST+* d0 and pD nuclei tracked on top of each other, with their 50% percentile ratios
372 near-identical to euploid nuclei [Fig. S7E,F]. In sum, these data indicate that *XIST* corrects T21
373 gene dosage in post-mitotic cell types via robust repression its chr21^{P} copy, especially in neurons,
374 whereas NPCs mitigate *XIST's* impact to some extent, likely due to continued passage through M
375 phase.

376 As our third metric for T21 dosage correction, we performed differential expression
377 analysis on variance-stabilized data [62], and compared effectively trisomic (*XIST*-negative pD and
378 nodox) nuclei to euploid (D21a/b), *XIST+* pD and d0 nuclei for each cell type. Indeed, generally
379 lower expression of chr21 in euploid relative to trisomic nuclei was also observed for *XIST+* pD
380 and d0 nuclei (Fig. S7G). Due to greater dispersion inherent in single-nuclei RNA-seq, the
381 moderated effect sizes (avg.log2FC) reflected in variance-stabilized data were smaller than in our
382 bulk RNA-seq (Fig. 2,4) but enabled comparing euploid to *XIST*-corrected T21 gene dosage.
383 Interestingly, *XIST* repressed chr21 genes to the near-euploid median, in all except 'Other' cell
384 types, which showed a small but significant residual excess expression (Wilcoxon p = 0.0007, Fig.
385 S8A). While the linear distance to the *XIST* transgene integration site did not correlate with mean
386 log2(FC) values in any of the d0+dox cell types, there was a distance effect in pD+dox neurons
387 and NPCs [Fig. S8B,C].
388 Importantly, differential expression of non-chr21 genes in *XIST*$^{+}$ d0 and pD nuclei
389 correlated strongly with log2(FC) values in euploid relative to effectively trisomic nuclei across all
390 cell type groups [Fig. 8E], with Pearson coefficients ranging from 0.25-0.46 in all except *XIST*$^{+}$ pD
391 NPCs. GSEA also reflected such transcriptome-wide reversion with strong NES correlations
392 between *XIST+* d0, pD and euploid conditions in MsigDB Hallmark and canonical pathways that
393 were significantly enriched (q-value ≤ 0.1) in euploid relative to effectively trisomic nuclei [Fig.
394 8F]. Again, the correlation in NPCs was lowest across all cell type groups, yet still significant
395 ($R=0.19$, $p=8.2\times10^{-7}$). Importantly, the vast majority of MsigDB Hallmark and canonical pathways
396 significantly enriched in any pairwise comparison (combined Fisher's method $p\leq1\times10^{-4}$) followed
397 the direction of change in the remaining third comparison [Fig. S8D]. In sum, these results
398 indicate that the degree of chr21 dosage correction in *XIST+* d0 and pD nuclei is sufficient to
399 revert T21 cells towards the euploid expression profile. We conclude that this new T21-*XIST*
400 transgene corrects chr21 dosage even in terminal and post-mitotic cell types, which will facilitate
401 detailed exploration of cellular and transcriptional T21 hallmarks that remain reversible after
402 completed development.
403
404

405 **DISCUSSION**

406 The relevance of the inducible T21-XIST system presented herein ranges from DS biology
407 and cellular responses to aneuploidy in general, to fundamental questions relating to human
408 *XIST*-mediated gene silencing and escape. In hiPSCs, our T21-XIST system is induced with near-
409 uniformity [Fig. 1] and corrects T21 dosage to euploid levels across chr21 [Fig. 2], which we
410 demonstrate by inclusion of isogenic euploid control hiPSCs lines we derived in parallel from a
411 male donor with mosaic T21 [36]. Leveraging phased sequence variants from linked-read WGS, we
412 can assign mRNA-seq reads allele-specifically to show that chr21 genes derive half of their
413 expression from the chr21^{P} allele in euploid (D21) cells, and one-third in T21 cells, but nearly
414 extinguish expression from this *XIST*-bearing copy after dox induction [Fig. 2].

415 *XIST*-mediated T21 dosage correction extends to genes responding to chr21 dosage on all
416 chromosomes, reflecting a transcriptome-wide reversion of gene expression that moves dox-
417 treated T21-XIST hiPSCs towards their isogenic euploid controls [Fig. 3]. A balanced experimental
418 design and stability of T21 silencing after dox withdrawal (w/d) enabled us to adjust for dox
419 effects that can inhibit mitochondrial translation [47] and selenocysteine incorporation [63]. GSEA
420 reflects the large-scale reversion of T21-responsive cellular components, pathways, and
421 functions [Fig. 3], including boosted expression of serine biosynthesis genes. These genes are
422 notable as dermal fibroblast of DS, as well as Patau (T13) and Edwards (T18) syndromes, depend
423 on serine for proliferation [20]. As such genes return to baseline upon correction of T21 dosage [Fig.
424 3], despite maintenance of the chr21 copy number, metabolic demand for serine, while common
425 to all three viable human autosomal aneuploidies, results from expression of the supernumerary
426 chromosome rather than its presence. We also find resurgent expression of ribosomal protein
427 genes and translation factors in T21-dosage corrected hiPSCs [Fig. 3], which may be due to a
428 resetting of the integrating stress response [14]. Indeed, cellular stress pathways and apoptosis are
429 dampened in response to T21 dosage correction, which is consistent with the previously reported
430 excess of apoptosis [17,51,52], mitochondrial dysfunction [18,48–50] and oxidative stress [16,53] in DS.

431 In T21-driven expression of neural cultures, we find many of the same terms are enriched
432 by GSEA and concordant with T21 hiPSCs [Fig. 4]. In keeping with a recent DS meta-analysis [64],
433 the interferon response [Fig. S4], as well as mitochondrial pathways and apoptotic terms [Fig.

434 S3], are particularly exacerbated in T21 neural cultures. Consistent with these results, we
435 demonstrate impaired survival of T21 forebrain neurons and interneurons relative to isogenic
436 euploid controls [Fig. 5], as well as reduced translation of EGFP [Fig. S5]. Because GSEA-enriched
437 terms and related genes responded to *XIST*-mediated T21 dosage correction in hiPSCs, they likely
438 reflect cellular phenotypes that depend on ongoing excess chr21 expression, and may therefore
439 remain amenable to T21 dosage correction after completed development.

440 During early neural differentiation, we observe that T21 NPCs produce an excess of
441 astrocytes at the expense of neurons [Fig. 6], which is consistent with astrogliosis noted in fetal
442 DS [28,30,32]. Because *XIST*-mediated T21 silencing remains inducible during differentiation and
443 persists into the NPC stage, neurogenesis is fully rescued when T21-dosage is corrected [Fig. 6].
444 This is consistent with a prior report using T21-*XIST* dosage correction [27], but we can attribute
445 this neurogenic rescue to suppression of a conserved T21 astrogenic bias, rather than slowed
446 commitment of T21 NPCs [Fig. 6]. We replicate this observation at the onset of cortical
447 astrogenesis in Ts65Dn embryos (E18.5), which indeed show a significant increase in S100B+ cells
448 relative to wildtype embryos, while the density of Ki67+ neural progenitors remains unchanged
449 [Fig. S6]. Several chr21 genes have been suggested to play a role in this astrogenic lineage bias,
450 including amyloid precursor *APP, S100B*, and *DYRK1A* [30,34]. In addition, it is possible that cellular
451 stress pathways impact NPC lineage decisions, as seen in rodent models of neurogenesis [65]. One
452 possible culprit may be oxidative stress that is elevated in DS hiPSC-derived neurons and NPCs
453 [40,66] and also implicates these and additional chr21 genes [16,30,53].

454 We also examined T21-*XIST* hiPSC-derived mature neural lineages after forcing NPCs to
455 terminally differentiate and thus commit to terminal neural cell fates via notch-inhibitor DAPT
456 [Fig. 7A,B]. This more mature (~9-12wk), post-mitotic neural population is composed of
457 terminally differentiated neurons and astrocytes, as well as residual neural progenitors and some
458 oligodendroglial lineages [Fig. 8, S6]. Remarkably, a large fraction of this terminal post-mitotic
459 population can induce *XIST* and attract repressive H2AK119ub on chr21 in response to dox [Fig.
460 7], regardless of whether they were never exposed to dox prior to cessation of the DAPT
461 treatment (post-DAPT, "pDAPT/pD"), or were treated with only a low ("LD", 1% of the standard

462 1 µM) dox concentration prior to DAPT treatment. In contrast, a previously reported T21-*XIST*
463 system could not be induced at all anymore in post-mitotic monolayer neural cultures [27].
464 Our results indicate our T21-*XIST* system represents a major improvement, which we
465 attribute to technical characteristics of transgene expression. First, our system uses a *UBC-rTTA*
466 construct integrated at the AAVS "safe-harbor" locus, in contrast to prior studies that used EF1a
467 [21] or CAG promoters [27] at this locus or re-delivered a high-copy *EF1α-rTTA* construct via piggyBac
468 to NPCs [67]. Second, there may be sequences differences in these human *XIST* cDNA constructs
469 that could impact the mature *XIST* RNA. And third, we integrated our *XIST* cDNA transgene
470 outside of *DYRK1A*, to minimize its impact on *DYRK1A* prior to dox treatment, but also to avoid
471 attracting gene-body associated DNAme from overlapping transcription, which serves to
472 suppress intragenic transcription start sites [68].
473 We assessed whether *XIST* induction in terminal, post-mitotic neural cell types ("pD") was
474 as effective in correcting T21 dosage as it was during differentiation ("d0") using three
475 independent analytic approaches: chr21^{P} allele representation, normalized expression across
476 chr21, and differential expression across the transcriptome [Fig. 8, S6, S7]. The chr21^{P} allele is
477 effectively repressed to nearly the same degree in *XIST+* pD as in d0 cells, especially in neurons.
478 [Fig. 8B,S6]. Likewise, both the median sum of normalized chr21 expression by cell, as well as the
479 entire distribution of cells, shift toward the euploid mean ratio [Fig. 8, S6]. The same significant
480 shift is observed when aggregating the mean ratio across cells for individual genes [Fig. 8, S6].
481 While some residual cycling NPCs retain excess expression in a subset of chr21 genes far (~20
482 Mbp) from the *XIST* integration site [Fig. S7], both normalized expression and allele-specific
483 metrics indicate *XIST* represses T21 dosage across all cell type groups, being most effective in
484 post-mitotic neurons. The transcriptome-wide analysis mirrors these results: differential
485 expression in *XIST*$^{+}$ d0 and pD cells correlates significantly with that of euploid cells when
486 compared to non-induced, *XIST*-negative T21 cells [Fig. 8E]. Likewise, canonical pathways
487 significantly enriched by GSEA in *XIST*$^{+}$ d0 and pD cells match and follow the direction of change
488 observed in the euploid to T21 comparison [Fig. 8, S7]. In sum, these data demonstrate for the
489 first time that post-mitotic terminal neural cell types remain responsive to chr21 gene dosage.
490 This motivates several avenues for future investigation, for example to dissect neuron-intrinsic -

491 and extrinsic phenotypes [69] that will be relevant for developing cell-type specific interventions [70],
492 or to identify pathways that remain amenable to novel therapeutic approaches [14].
493 Regarding *XIST* biology, our results suggest human neural lineages remain competent to
494 initiate *XIST*-mediated heterochromatin deposition even non-cycling cells, provided *XIST* can be
495 induced. Similar developmental plasticity in initiating [25,26], or re-initiating [71,72] *XIST*-mediated
496 repression was previously reported only for proliferative hematopoietic cell lineages. Our work
497 therefore suggests *XIST* may be able to re-establish X chromosome inactivation even outside
498 pluripotency and hematopoiesis, which is relevant to recently reported X chromosome
499 conformational changes in the female brain across the estrous cycle [73].
500 Additionally, prior reports of *XIST* induction in human HT1080 fibrosarcoma cells indicate
501 that spreading of autosomal gene silencing remains reversible [74] and remains only effective near
502 its site of integration [75]. Both of these observations may be impacted in part by *XIST* repressing
503 haploinsufficient genes, which are not uncommon on mammalian autosomes, making whole or
504 partial trisomy a valuable research tool to better understands the determinants of *XIST* spreading
505 [76]. In hiPSCs, our T21-XIST system repressed virtually every chr21-linked gene without
506 measurable impact of its linear distance from the *XIST* integration site across a large span of
507 expression values, and in irreversible fashion [Fig. 2]. Interestingly, the human inactive X in
508 pluripotent stem cells frequently undergoes progressive reactivation following loss of *XIST*
509 expression [77], the order of which we recently showed was determined in part by the distance to
510 the nearest escapee gene [78]. While our T21-*XIST* dox withdrawal was limited to 3-6 weeks, we
511 found little evidence of reactivation over this period, indicating that DNA methylation served to
512 maintain T21 silencing [Fig. 2]. Whether this remarkable epigenetic stability was due to the
513 paucity of chr21 genes escaping *XIST* to seed potential reactivation, or the levels of *XIST* prior to
514 dox withdrawal, and to which degree these two aspects are related, represent additional areas
515 for future investigation.
516
517
518
519

520 **FIGURE LEGENDS**

521

522 **Figure 1: T21 hiPSCs induce *XIST* transgene and deposit heterochromatin on one chr21 allele**

523 (A) Schematic of cell lines and sample collection timepoints and dox treatment conditions.
524 Samples were collected after 3-9 wks of +dox or no-dox treatment, or 3 wk of +dox and 3 or 6
525 wks of dox withdrawal. A subset of samples was treated with dox for 2mo+ prior to
526 collection/withdrawal.

527 (B) Representative images (left) for XIST-FISH, and H2AK119ub and H3K27me3 IF, and image
528 quantification (right). Control panel of XIST-negative cells after 3wk of dox w/d for XIST-FISH is
529 included on the left.

530 (C) *XIST* expression in T21-XIST samples from mRNA-seq (VST, variance-stabilized
531 transformed counts, approaching a log-transformation).

532

533 **Figure 2: *XIST*-mediated silencing extends across entire chr21^{P} and attracts DNAme**

534 (A) Representation of M/M2 and P alleles of all protein-coding chr21 genes across dox
535 conditions and genotypes. Thick black line at 0.5 marks expected biallelic expression in euploid
536 (D21) cells, and dashed thin black line expected 1/3rd representation for chr21^{P} allele in T21 cells.

537 (B) Heatmap showing VST counts normalized to the mean count in T21 samples (left panels)
538 for all expressed genes on chr21.

539 (C) Distribution of log2(FC) (log2-foldChange) relative to no-dox T21 samples, for all
540 differentially expressed genes (DEGs, p.adj≤0.1). "Combined" represents the differential
541 expression condition used in subsequent figures. Blue and green shaded bands correspond to
542 ±10% and ±0.15 variation from a log2(FC) of -0.59 (dashed vertical line, log2FC expected for
543 complete T21 dosage correction).

544 (D) Log2(FC) values across chr21 genes (arranged by position) compared to T21 samples.
545 Bubble colors shaded as indicated in the legend above, bubble size reflects base mean
546 expression.

547 (E) As in (B), displaying only genes that maintain a LAF ≥ 1/6th in allelic T21 mRNA-seq in +dox
548 or w/d conditions.

549 (F) Distribution of DNAme values from promoter-associated methylEPIC probes on chr21
550 genes in T21-XIST no-dox, +dox, and w/d. Bimodal distribution medians of probes > and ≤ 60%
551 methylated displayed on their respective peaks.
552
553 **Figure 3: Transcriptome-wide response to T21 gene dosage and correction via *XIST***
554 (A) Fraction of genes differentially expressed in response to T21 (top, relative to euploid) and
555 T21-XIST dosage correction (bottom, relative to T21 and no-dox) by direction (increasing,
556 decreasing, or unchanged, ~0) and by chromosome.
557 (B) PCA of all mRNA-seq samples, batch-corrected for timepoint and dox status. Open
558 symbols for original euploid (198-1/2) and T21 (198-5) lines, filled symbols for T21-XIST transgenic
559 lines (c1/4/7). Colors indicate effective chr21 dosage as indicated in Figures 1 and 2 (w/d colored
560 separately to distinguish from +dox T21-XIST samples).
561 (C) Overlap of differential expression between hiPSC T21/D21 (y-axis) over the dox effect
562 (left, non-transgene +dox/no-dox) or T21-XIST dosage correction (right, T21XIST+dox &
563 withdrawal / T21). Adjusted p-values combined by Fisher's method (C.padj) for all DEGs, and
564 colored by -log10(C.padj) provided C.padj ≤0.1. Linear regression plotted with the Spearman
565 correlation coefficient and p-value for all genes.
566 (D) Overlap of enriched GSEA terms comparing normalized enrichment scores (NES) for hiPSC
567 T21/D21 over dosage-corrected T21-XIST/T21. Bubbles correspond to the -log10(combined
568 pvalue by Fisher's method). Colors denote chosen categories (all with combined pvalue ≤ 0.2).
569 (E) Individual significantly-enriched terms (combined p≤0.1) from each of the categories in
570 (D), selected by concordance measure (Euclidean distance from origin in D). Colors denote NES,
571 bubble size the individual -log10(p.adj).
572
573 **Figure 4: Concordant T21 dosage imbalance and transcriptomic response after neural**
574 **differentiation**
575 (A) Heatmap showing VST counts normalized to the mean count in T21 neural samples (left
576 panels) for all expressed genes on chr21.

577 (B) Distribution of log2(fold-change) from chr21 genes comparing neural T21 to D21. Dashed
578 black line denotes expected log2(FC) of +0.59 (includes all chr21 genes, irrespective of p.adj).
579 (C) Overlap of differential expression between hiPSC T21/D21 (y-axis) over neural T21/D21
580 samples (x-axis). Adjusted p-values were combined and colored as in Fig. 3C, with linear
581 regression line (dashed, with Spearman coefficient and p-value for all genes with c.padj ≤ 0.1).
582 (D) Overlap of enriched GSEA terms comparing normalized enrichment scores (NES) for hiPSC
583 T21/D21 (y-axis) over neural T21/D21. Bubble plots corresponds to the -log10(combined pvalue
584 by Fisher's method). Colors denote chosen categories (all with combined pvalue ≤ 0.2).
585 (E) As in (D) but combining neural T21/D21 GSEA (x-axis) with GSEA of dosage-corrected T21-
586 XIST hiPSCs (hiPSC rescue) on the y-axis.
587
588 **Figure 5: Increased cell death of T21 relative to euploid interneurons and forebrain neurons**
589 (A) Representative sequence of a TS21 interneuron labeled with RGEDI-P2a-EGFP dying
590 over the course of imaging and a control neuron surviving during the course of imaging
591 (scale/width is 10 µm).
592 (B) Plot of the cumulative rate of death of TS21 and control interneurons. Step functions
593 correspond to the mean cumulative death rate across wells per line and the faint lines
594 represent each well replicate (n = 6 wells each, HR = 4.08, Linear mixed model with Holm
595 correction, ** *p* <0.01). C) as in B) for the cumulative rate of death of TS21 and control
596 forebrain neurons (n = 6 wells each, HR = 2.57, Linear mixed model with Holm correction, ** *p*
597 <0.01).
598
599 **Figure 6: Early astrogenesis at neurogenic expense is suppressed by T21 dosage correction prior**
600 **to NPC stage**
601 (A) Representative images (left) and quantification (right) of H2AK119ub (IF) and XIST (FISH)
602 signal after neural differentiation from dox treated cells. Dox treatment initiated while cells were
603 hiPSCs (left top), or on the first day of differentiation ("d0", left bottom).
604 (B) Relative lineage commitment to astrocytes (S100b) or neurons (MAP2) in euploid, T21,
605 and T21-XIST cells under dox treatment. Symbols (Wilcoxon two-tailed p-value level, or "ns" for

606 p > 0.1) above each boxplot denote significance of median difference from the corresponding
607 euploid (198-1/2) condition, whereas symbols below each boxplot compare to T21 (198-5)
608 lineage proportions.
609 (C) Representative images at d28 of neural differentiation in euploid (left column), trisomic
610 (center column) and rescued (right column) labeled for neuronal MAP2 (red), astroglial S100B
611 (green) and H2AK119ub accumulating on chr21 (white). Insets (labeled 1,2) display H2AK119ub
612 foci in both astrocytes and neurons.
613
614 **Figure 7: Post-mitotic neurons and astrocytes can induce *XIST* and deposit H2AK119ub after**
615 **terminal lineage commitment**
616 (A) Sample and timeline schematic of XIST induction during (d0+dox) and after terminal
617 neural differentiation post DAPT treatment (pD+dox). Cell cycle exit of NPCs is assessed by EdU-
618 labeling of S-phase transiting cells, with co-detection of *XIST* by FISH after 2 days in dox media.
619 Chr21 Barr body formation (H2AK119Ub) and lineage commitment (MAP2/S100B) are assessed
620 by IF in 8 wk and 10-12 wk cultures.
621 (B) Representative *XIST* (red) and EdU (green) image and quantification of d36 neural
622 differentiation following 4d of DAPT and 2d of dox treatment. Less than 6% of cells were EdU+
623 (green), EdU+XIST+ cells represented less than 2% of total cells.
624 (C,D) Representative images (C) and quantification (D) of H2AK119ub (yellow) IF and XIST-FISH
625 (red) signal after neural differentiation from different dox treatments. Bottom pDAPT panel
626 shows H2AK119ub IF (white) co-stained with MAP2 (red) and S100B (green).
627
628 **Figure 8: Effective monoallelic repression of chr21 genes by *XIST* induced in terminal neurons**
629 **and astrocytes**
630 (A) Single-nuclei RNA-seq UMAP of terminal 10-12 wk neural cultures (as outlined in Fig. 7A).
631 Integrated UMAP colored by original clusters, granular and grouped cell types, cell cycle stage,
632 XIST count categories and samples.
633 (B) Paternal allele fraction by cell, aggregated over all chr21 genes. Cells are split by sample
634 (D21a/b, T21XIST-nodox, d0+dox, pD+dox) and *XIST* status (0, >1 counts denoted “X-“ and “X+”),

635 except for euploid lines (absent XIST transgene, grey). Median paternal allele fraction and
636 significance of difference in medians relative to T21-nodox cells (Wilcoxon p-value) are denoted
637 below and above boxplot, respectively.
638 (C) Normalized gene expression ratio (chr21 over genome mean excluding chr21) by cell,
639 aggregated over all chr21 genes. Cells are split as in B (excluding cell type group "Other"), with
640 median expression ratio and difference in medians relative to T21-nodox cells (Wilcoxon p-value)
641 denoted above and below boxplot, respectively.
642 (D) Normalized expression ratio by chr21 gene, aggregated over cells. Mean ratios per gene
643 calculated from cells are split as in C. Respective median expression ratios and difference in
644 medians relative to T21-nodox cells (Wilcoxon p-value) denoted above and below boxplots.
645 (E) Differential expression of non-chr21 genes relative to XIST-negative postDAPT and T21-
646 nodox cells. Sample-averaged log2(FC) values in euploid cells (x-axis) correlate with XIST-positive
647 d0 and pDAPT log2(FC) values (y-axis), faceted by cell type group. Colors and transparency denote
648 respectively, ROC power and ROC power of the euploid relative to T21 comparison. Regression
649 line (black), Pearson coefficient and p-value (Fisher-transformed) denoted on each plot.
650 (F) GSEA results of differential expression comparisons depicted in (E), correlating
651 normalized enrichment scores (NES), and plotted as in (E). Plotted MSigDB gene sets limited to
652 Hallmark and Canonical pathways subsets significant (q-value ≤ 0.1) in T21/euploid comparison
653 (x-axis). Colors and transparency denote respectively, -log10-transformed q-values of each
654 comparison and the euploid to T21 comparison. Regression line (grey), Pearson coefficient and
655 p-value (Fisher-transformed) denoted on each plot.
656
657
658
659
660
661
662
663

664 **SUPPLEMENTARY FIGURE LEGENDS**

665 **Figure S1**

666 (A) Taqman copy number (CN) assay for 21q22 (*DYRK1A*) in GM00260-derived hiPSC clones.

667 (B) Taqman CN assay for 17q25 (*SEC14L1*) in GM00260-derived hiPSC clones.

668 (C) DNA SureFISH for chr21q, and FastFISH chrX, chr8, chr12, and chr17 centromeres in 198-
669 6/8 with counts and images denoting the dominant staining pattern.

670 (D) Summary of CytoSNP850k calls across GM00260 and its reprogrammed hiPSC clones. Calls
671 marked with a red 'x' were common across all lines, including donor fibroblasts. Call marked with
672 a small 'x' were line-specific, except for T21 (denoted by a capital 'X').

673 (E) Absolute difference in allele (theta) frequency of CytoSNP850k probes comparing T21 and
674 euploid clones (D21), colored by T21-specific base calls (red/blue) and hetero/homozygosity
675 (grey and yellow, respectively).

676 (F) DNA FISH against DSCR8 (Vysis, LSI21) in interphase and metaphase spreads of validated
677 hiPSC clones, with counts and images denoting the dominant staining pattern.

678 (G) Taqman CN assay for 21q22 (*DYRK1A*) across all AAVS-rTTA subclones of T21 198-5 hiPSCs.

679

680 **Figure S2**

681 (A) Germ layer-specific and pluripotency marker expression across the euploid (198-1/2), T21
682 (198-5), and transgenic T21-XIST (c1/4/7) hiPSC lines.

683 (B) Change in log2-transformed expression relative to corresponding T21 samples in this and
684 the two referenced T21-XIST studies. Mean difference of chr21 gene expression comparing w/d
685 T21-XIST samples and T21 samples. Line type denotes the length of the initial dox treatment, and
686 color the duration of dox w/d.

687 (C) Mean difference of chr21 gene expression between w/d T21-XIST and T21 samples. Line
688 type denotes the length of the initial dox treatment, and color the duration of dox w/d.

689

690 **Figure S3**

691 (A) Same as Fig. 3C but excluding chr21 genes: overlap of differential expression between
692 hiPSC T21/D21 (y-axis) over the dox effect (top, non-transgene +dox/no-dox) or T21-XIST dosage

693 correction (T21XIST+dox & withdrawal / T21). Adjusted p-values were combined (C.padj,
694 calculated using Fisher's method), and colored by -log10(C.padj) provided C.padj ≤0.1 (or grey for
695 C.padj > 0.1). Linear regression is plotted along with the Spearman correlation coefficient and p-
696 value for all non-chr21 genes.
697 (B) Individual significantly-enriched terms (combined p ≤ 0.1) from each of the categories in
698 Fig. 4(D,E), selected by a concordance measure (euclidean distance from origin in D). Colors
699 denote NES, bubble size the individual -log10(p.adj).
700
701 **Figure S4**
702 Comparison of terms over-represented in GSEA across hiPSC T21, neural T21, T21 dosage
703 correction ("rescue"), and the dox-effect in non-transgenic hiPSCs. Terms from Hallmark, KEGG,
704 and WikiPathways (WP) are shown. All terms are sorted by hiPSC T21 NES (normalized
705 enrichment score from GSEA), with a p.adj thresholds of p ≤ 0.1 for hiPSC T21, and additionally
706 p.adj ≤ 0.2 for the three additional panels (neural T21, T21 rescue, and dox-effect).
707
708 **Figure S5**
709 (A) Representative images of TS21 interneuron and euploid control cultures transduced
710 with hSyn1:RGEDI-P2a-EGFP lentivirus. Scale bar = 100 µm.
711 (B) Quantification of the GEDI ratio (mean RGEDI/mean EGFP) across each interneuron per
712 time point (T21 n= 8810, D21/euploid control n= 15,999). Live/dead threshold of 0.15 (red line)
713 (C) as in (B), but across each forebrain neuron per time point (T21 n= 30,735, D21/euploid
714 control n= 24,950).
715 (D) Number of cells tracked by segmentation in independent wells of T21 and D21 neurons
716 across all timepoints.
717 (E) Fluorescence intensity signal of RGEDI, EGFP and RGEDI/EGFP ratios in live (RGEDI/EGFP
718 ratio < 0.15) T21 and euploid control neurons ($p \leq 1x10^8$, linear mixed model with Holm
719 correction).
720 (F) Anti-GFAP (red) and DAPI (blue) staining of cultures from (A) showing abnormal glia
721 morphology. Scale bar = 300 µm.

722 **Figure S6**

723 (A) S100B$^+$ cell density and representative images of E18.5 wildtype and Ts65dn cortical
724 slices (100 µm scale bars). Two-tailed, independent samples Student's t-test $p \leq 0.05$ (*).

725 (B) Ki67$^+$ cell density and representative images of E18.5 wildtype and Ts65dn cortical slices
726 (60 µm scale bars). Two-tailed, independent samples Student's t-test $p > 0.05$ (n.s.).

727

728 **Figure S7**

729 (A) Sample proportions (% nuclei) of assigned cell types, cell cycle stage and *XIST* status
730 faceted by cell type group.

731 (B) Paternal allele fraction by cell, aggregated over all chr21 genes, and faceted by cell type
732 group. Cells split by sample (D21a/b, T21XIST-nodox, d0+dox, pD+dox) and *XIST* status (0, >1
733 counts denoted "X-" and "X+"), except for euploid lines (absent XIST transgene, grey). Median
734 paternal allele fraction and significance of difference in medians relative to T21-nodox cells
735 (Wilcoxon p-value) are denoted below and above boxplot, respectively.

736 (C) Left: Normalized gene expression ratio (chr21 over genome mean excluding chr21) by cell,
737 aggregated over all chr21 genes, and faceted by cell type group. Cells are split as in B, with median
738 expression ratio and difference in medians relative to T21-nodox cells (Wilcoxon p-value)
739 denoted above and below boxplot, respectively. Right: empirical cumulative distributions (eCDF)
740 of corresponding panels on the left, colored by sample and XIST-positive cells represented by
741 dashed lines. T21-nodox 95% confidence interval denoted by transparent ribbon (purple).
742 Sample-colored p-values (Kolmogorov-Smirnov, KS-test) denotes significance of distribution of
743 shift from the T21-nodox sample. Grey lines indicate the 50th percentile cell (horizonal), and chr21
744 to genome-wide mean ratio (vertical 1.0 and 1.5).

745 (D) Left: Normalized expression ratio by chr21 gene, aggregated over cells, and faceted by
746 cell type group. Mean ratios per gene calculated from cells are split as in C. Respective median
747 expression ratios and difference in medians relative to T21-nodox cells (Wilcoxon p-value)
748 denoted above and below boxplots. Right: eCDF of corresponding panels of the left, with lines
749 colored as in C. T21-nodox confidence-interval, sample-colored p-values (KS-test) and grey
750 vertical lines s in C, with the horizontal grey line indicating the 50th percentile chr21 gene.

751 (E,F) Cumulative distributions aggregating across cell type groups (right panels in C & D),
752 excluding the "Other" group. Lines, sample-colored p-values (KS-test), grey horizontal and
753 vertical lines as in C and D, respectively.
754 (G) Differential expression of chr21 genes relative to XIST-negative postDAPT and T21-nodox
755 cells. Average log2(FC) values in euploid cells (x-axis) correlate with XIST-positive d0 and pDAPT
756 log2(FC) values (y-axis), faceted by cell type group. Colors and transparency denote respectively,
757 ROC power and ROC power of the euploid relative to T21 comparison. Regression line (black),
758 pearson coefficient and p-value (Fisher-transformed) denoted on each plot.
759
760 **Figure S8**
761 (A) SC-transformed sample-averaged log2(FC) values relative to XIST-negative T21-nodox
762 and pDAPT cells faceted by cell type group. Median sample-averaged log2(FC) values of euploid
763 (D21a/b), and XIST-positive d0+dox and pD+dox samples, and significance of median differences
764 (Wilcoxon p-value) from T21 to euploid comparison denoted below and above corresponding
765 boxplot.
766 (B) Loess-smoothened SC-transformed log2FC values of differential expression comparisons
767 (as in A, with 95% confidence intervals) across chr21 coordinates of transcriptional start sites
768 (TSS, in Mbp).
769 (C) SC-transformed sample-averaged log2(FC) values of d0+dox and pD+dox comparisons
770 (colored as in A,B) plotted over the TSS distance from the *XIST* transgene integration site, faceted
771 by cell type group. Regression lines, 95% confidence interval ribbons, pearson coefficient (R), and
772 p-value (fisher-transformed R) indicated on each plot, black horizontal line denotes no change.
773 (D) Normalized enrichment scores (NES, x-axis) of GSEA against Hallmark and Canonical
774 pathways MSigDB subsets in euploid (center) and XIST-positive d0+dox and pD+dox cells. Plotted
775 categories (y-axis) limited to significant enrichment across at two comparisons (pairwise Fisher's
776 method combined p-value ≤ 0.005). Colors and transparency denote respectively, NES sign and -
777 log10-transformed q-values (capped at 3, q <= 0.001).
778
779

780 **MATERIALS & METHODS**

781

782 ***EXPERIMENTAL DESIGN***

783 **Reprogramming, hiPSC validation and culture**

784 Human male fibroblast line (GM00260) mosaic for trisomy 21 (T21) was obtained from
785 the Coriell Institute (Camden, NJ) and reprogrammed by the University of Connecticut's Cell and
786 Genome Engineering Core, using the CytoTune hiPSC 2.0 Sendai Reprogramming kit (Thermo
787 Fisher Scientific, Waltham, MA). Genomic DNA from hiPSC clones was screened via duplex
788 Taqman Copy Number (CN) Assay (*DYRK1A* - Hs01748441_cn and RNaseP, Thermo Fisher
789 Scientific) to select euploid and T21 lines, followed by additional screening for Chr17q Taqman
790 CN assay (*SEC14L1*, Hs05476397_cn), and the hPSC Genetic Analysis Kit (Stemcell Technologies,
791 Vancouver, Canada). Interphase and M phase nuclei were also screened via FASTFISH (WiCell,
792 Madison, WI) using Chr 20q (BCL2L1) and centromere enumeration probes for Chr 8, 12, 17, and
793 X, alongside a SureFISH assay for Chr 21q (DSCR8). Selected hiPSC lines were further screened by
794 aCGH (Infinium BeadChip CytoSNP 850K assay, Illumina, San Diego, CA) at the Center for Genome
795 Innovation, Institute for Systems Genomics at the University of Connecticut.

796 T21 and euploid hiPSCs were cultured on mitotically inactive mouse embryonic fibroblasts
797 (mEFs) in standard hiPSC media in 5% CO_2 at 37°C (80% DMEM/F12, 20% Knockout Serum
798 Replacement, 1% Glutamax, 1% Non-Essential Amino Acids, 0.1% ß-Mercaptoethanol, and 8
799 ng/mL bFGF, Thermo Fisher Scientific), and passaged weekly by manual disruption of 6-10
800 representative colonies. For hiPSC cultures requiring doxycycline induction, 2 µM doxycycline
801 was added to the culture media.

802

803 **Plasmid construction**

804 For PCR amplifications, either Herculase II polymerase (Agilent, Santa Clara, CA), Platinum
805 Taq High Fidelity (Thermo Fisher Scientific), Advantage 2 polymerase (TaKaRa Bio, Shiga, Japan),
806 or Q5 Hi-Fidelity DNA Polymerase (New England Biolabs) was used. For cloning reactions except
807 the large *XIST* insert steps, ligations were performed with T4 DNA ligase, 2,000,000 units/mL
808 (New England Biolabs) and DH10B homemade chemically competent cells were used at 37°C. For

809 all cloning with XIST cDNA fragments aside from ligation of oligo not followed by transformation
810 (which used the same T4 DNA ligase), the TaKaRa DNA Ligation Kit LONG (TaKaRa Bio) was used
811 along with NEB Stable Competent E. coli (New England Biolabs) with bacterial incubations at 25-
812 30°C to mitigate instability in initial steps observed at 37°C.

813 To clone the XIST transgene cDNA in a temporary pUC19 vector, a 10 kb fragment
814 containing most of XIST exon 1 was cut from a fosmid (WI2-935P22, BACPAC Genomics) with SacII
815 and PshAI. Linker oligos were used to clone the 10 kb SacII and PshAI fragment into the KpnI and
816 XbaI sites of pUC19, respectively. The 5'-most end of *XIST* exon 1 was PCR amplified, concurrently
817 adding a 5' PmeI restriction site. The resulting PCR product was digested with PmeI and BtgZI and
818 cloned in between the PmeI/BtgZI restriction sites of the XIST exon 1-containg plasmid. The 3'
819 end of exon 1 through exon 6 was amplified from cDNA of Wi-38 cells (AG07217, Coriell Institute),
820 while adding a 3' SalI restriction site. The resulting PCR was digested with PshAI and SalI and
821 cloned between the PshAI and SalI sites of the plasmid from the prior step to complete the XIST
822 cDNA construct. The *UBC* promoter from the FUGW construct [79] (Addgene plasmid #14883) was
823 cloned into AAVS1-Neo-M2rtTA [80] (Addgene plasmid #60843). The *UBC* promoter was PCR-
824 amplified with flanking PvuII and FseI sites, and cloned into the AleI and FseI sites on the AAVS1-
825 neo-M2rtTA plasmid. This rtTA-advanced ORF was replaced with rtTA3G from the pCMV-Tet-3G
826 plasmid (TaKaRa Bio), by XbaI and XmaI digestion and cloning of three separate fragments to
827 create the final rtTA vector AAVS1-NEO-UBrtTA-3G.

828 To generate the final targeting vector, pTRE3G (TaKaRa Bio) was used as the backbone,
829 following excision of an XbaI fragment to reduce the size of the vector via removal of the SV40
830 small intron, NLS, and SV40 polyA sequences. The 5' homology arm for chr21 was generated by
831 PCR with EcoRI sites on each primer using the genomic DNA of the destination cell line as the
832 template. This PCR product was ligated into the EcoRI sites of the pTRE3G vector to
833 make pTRE3G-5P. Next a fusion PCR product was generated, harboring a BGH polyA amplified
834 from pl452 [81] and the 3' homology arm using overlapping PCR from the genomic DNA of the
835 destination cell line. This PCR product was cloned into the PstI and BamHI sites of the pTRE3G-
836 5P to make pTRE3G-5P3P. Next a loxP-flanked PGK-puro-TK fragment was removed from
837 vector pl452-puroTK by XhoI digest. The fragment was cloned into the XhoI sites of the

838 vector pTRE3G-5P3P. This pl452-puroTK vector was derived from plasmids pl452 and
839 plasmid pLCA.66/2272 [82] (Addgene plasmid #22733) by removing the PGK-puroTK cassette with
840 AgeI and BbsI and cloning that fragment into pl452 using the same enzymes. To add the *XIST*
841 cDNA construct, this CMV-puroTK-TRE3G vector was digested with MluI and SbfI, and a
842 phosphorylated linker oligo was ligated to purified, digested backbone, creating a SacI-
843 compatible overhang. Following purification, this vector was ligated to the SbfI-SacI fragment
844 containing the *XIST* cDNA construct, to create the TRE3G-XIST cDNA targeting vector.
845
846 **hiPSC targeting and screening**
847 Targeting was performed using a Lonza Nucleofector 4D (Lonza, Basel, Switzerland) with
848 primary cell kit P3 and program CD-150. AAVS1-Neo-ubrtTA was targeted to chr21 of the T21
849 cell line 198-5. Two µg of each AAVS1-targeting TALEN [83] was nucleofected along with 6 µg of
850 AAVS1 integration vector. Cells were plated on mitotically inactivated DR4 MEFs (ATCC,
851 Manassas, Virginia) post-nucleofection. After 96 hours, cells were cultured with G418 at a
852 concentration of 25 µg/ml. Selection was done for a total of 6 days. Resulting colonies were
853 isolated and screened for targeting. cDNAs from targeted clones were tested for expression of
854 rtTA by RT-qPCR. AAVS1 TALEN-L (Addgene plasmid #59025) and AAVS1 TALEN-R (Addgene
855 plasmid #59026) [84] were used for targeting the UBrtTA . Integrants were screened using (AAVS1
856 scr F/Neo R and AAVS1 3'scr R/rtTA F). For targeting XIST transgene via CRISPR, guides designed
857 to target the chr21P copy without cutting the chr21$^{M/M2}$ alleles were cloned
858 into PX459V2 (Addgene plasmid #48139) [85] at the BbsI site by annealing and ligating overlapping
859 oligos. Two µg each this CRISPR guide plasmid was used along with 6 µg XIST cDNA targeting
860 vector. Cells were plated on DR4 MEFs and after 96 hours, puromycin was added to the culture
861 at a concentration of 0.5 µg/ml for a total of 4 days. Resulting colonies were isolated and
862 genotyped for targeting by PCR. Clones were verified by sequencing across the target to verify
863 the loss of the targeted allele.
864
865
866

867 **Nucleic acid purification**

868 Genomic DNA was purified from fresh or frozen pelleted cells using three different
869 methods depending on application. For colony PCR screening, genomic DNA was extracted via
870 standard high-salt chloroform extraction. For standard PCR, and array hybridization, cell pellets
871 were resuspended in either cell lysis buffer 1 (10 mM Tris-HCl, pH 8.0; 100 mM NaCl; 10 mM
872 EDTA, pH 8.0; 1% SDS; 200 µg/ml Proteinase K), or cell lysis buffer 2 (10 mM Tris-HCl, pH 8.0; 200
873 mM NaCl; 10 mM EDTA, pH 8.0, 0.5% Sarcosyl; 1 mg/mL Proteinase K) and incubated at 55°C for
874 3 hours to overnight with optional RNAse A, 10 µg/mL treatment following at 37C for 5 minutes.
875 Genomic DNA was isolated using Phenol:Chloroform:Isoamyl Alcohol (25:24:1, v/v) (Invitrogen,
876 Waltham, MA), precipitated with either isopropanol or 300 mM sodium acetate with 2 volumes
877 of 100% chilled ethanol and 15 minutes at -80C, washed with 70% ethanol, and resuspended in
878 TE buffer. For linked-read WGS, high molecular weight (HMW) genomic DNA was prepared from
879 fresh or frozen hiPSC cell pellets, following the protocol listed in the Chromium Genome Reagent
880 Kits v2 User Guide (10x Genomics, Pleasanton, CA), using the MagAttract HMW Kit (Qiagen,
881 Germantown, MD) with minor modifications. Plasmid and fosmid DNA was purified with either
882 the Zyppy Plasmid Miniprep kit or ZymoPURE II Plasmid Midiprep kit (Zymo Research, Irvine, CA).
883 Following restriction digests or PCR, DNA purification was performed with the Monarch PCR &
884 DNA Cleanup kit (New England Biolabs, Ipswich, MA), or the DNA Clean & Concentrator Kit (Zymo
885 Research). For RNA isolation, the PureLink RNA Mini Kit (Invitrogen, Carlsbad, CA) was used,
886 followed by cDNA synthesis using the iScript gDNA Clear cDNA Synthesis Kit (Bio-Rad
887 Laboratories, Hercules, CA).

888

889 **Quantitative RT-PCR**

890 Gene expression was measured via quantitative real-time PCR (qRT-PCR) using the iTaq
891 Universal SYBR Green Supermix (Bio-Rad Laboratories) and the ΔCt method. Primer specificity
892 was confirmed by melting curve analysis, and relative expression was calculated as %GAPDH
893 ($100/2^{\Delta Ct}$). Taqman CN assays were normalized to 198-1 genomic DNA. HOT FIREPol Probe
894 Universal PCR Mix Plus - no ROX (Solis BioDyne, Tartu, Estonia) was used per manufacturer's
895 instructions, using 4 ng of high-quality genomic DNA template in 20 µl reactions. The hPSC

896 Genetic Analysis Kit (Stemcell Technologies) was used following the manufacturer's instructions.
897 All qPCR reactions were performed in triplicate in a Bio-Rad CFX 96 Real-Time System.
898
899 **Cytogenomics, DNA methylation, Linked-read WGS and mRNA sequencing**
900 For cytogenomic analysis, genomic DNA was labeled and hybridized to the Infinium
901 BeadChip CytoSNP 850K array (Illumina, San Diego, CA) according to the manufacturer's
902 protocols. For DNAme analysis, genomic DNA was bisulfite-converted using the EZ DNA
903 Methylation Kit (Zymo Research, Irvine, CA), then labeled and hybridized using the Infinium
904 Methylation EPIC BeadChip Kit (Illumina) following standard protocol of each manufacturer. Both
905 types of arrays were scanned on a NextSeq 550 system (Illumina). HMW genomic DNA was
906 sequenced to ~30x coverage on a NovaSeq 6000 (Illumina), following library preparation on the
907 10X Genomics Linked-Read platform at the Center for Genome Innovation, Institute for Systems
908 Genomics at the University of Connecticut. For standard mRNA-seq, libraries were prepared
909 using the Illumina stranded mRNA Kit and 100bp paired-ends reads were sequenced to an
910 average depth pf 40 million reads/replicate on the NovaSeq 6000 (Illumina, San Diego, CA).
911
912 **Immunofluorescence and XIST RNA-FISH**
913 For *XIST* RNA FISH, cells were permeabilized with 0.5% Triton-X and 2mM ribonucleoside
914 vanadyl complex (RVC) in CSK Buffer (10mM PIPES pH 6.8, 100mM NaCl, 3mM MgCl2, 300nM
915 sucrose), fixed in 4% PFA in PBS, then dehydrated through a series of ethanol washes (70%,80%,
916 90%, and 100%). Digoxigenin-labeled *XIST* probe hybridization was performed overnight in a
917 humidity chamber at 42°C. Anti-digoxigenin antibody (ThermoFisher; 700772) was hybridized for
918 1 hour at RT. Secondary antibody hybridization (Alexa Fluor; Invitrogen; 1:500) followed for 1
919 hour at RT. Nuclear DNA was counter-stained with Hoechst 33342 dye. Slides were imaged with
920 an EVOS FL Auto2 system (Thermo Fisher Scientific).
921 For immunofluorescence cells were grown in Nunc Lab-Tek II glass chamberslides coated
922 with poly-d-lysine and laminin (for neural differentiation) or permanox chamberslides with MEFs
923 (iPSCs). Cells were fixed in 4% paraformaldehyde (Electron Microscopy Sciences, Hatfield, PA) for
924 10 minutes at room temperature (RT), rinsed with PBS 3 times for 5 minutes and then

925 permeabilized in 1% Triton-X in PBS for another 10 minutes. Samples were blocked in blocking
926 buffer containing PBS, 0.1% Triton-X, 5% BSA and 2% normal goat serum (MilliporeSigma). Cells
927 were placed in antibodies diluted in blocking buffer overnight at 4°C in a humidity chamber.
928 Primary antibodies were used as follows: MAP2 (Abcam; ab5392; 1:10,000), S100B (Sigma; s2532;
929 1:1000), H2AK119ub (Cell Signaling; 8240, 1:1600). Following washes in 0.1% Triton-X in PBS, 3
930 times for 5 minutes, cells were labeled with Alexa Fluor secondary antibodies at 1:500 for 1 hour
931 at RT. Nuclei were counterstained with Hoechst 33342and slides preserved in Prolong Gold
932 Antifade Mountant (Thermo Fisher Scientific).
933
934 **Neural differentiation**
935 T21 and euploid hiPSCs were passaged manually onto mEFs and in hiPSC medium. On day
936 2 post-passage, cultures were switched into N2B27 neural differentiation medium (Neurobasal
937 medium (Gibco), 2% B27 (Gibco), 1% N2(DMEM:F12 (Gibco), 25 µg/ml insulin (Sigma), 100 µg/ml
938 holo-transferrin, 100 µM putrescine, 20nM progesterone, 30nM selenite), 1% ITS-A (Gibco), 1%
939 Penicillin-Streptomycin (Gibco), and 1% Glutamax (Gibco), supplemented with noggin at 500
940 ng/ml (R&D Systems). Cultures were fed and supplemented with Noggin every other day through
941 day 10. For neural differentiation with doxycycline induction, 1 µM doxycycline, or 0.01 µM for
942 low-dose cultures, was added to the culture media. Cultures were fed N2B27 until the
943 appearance of mature rosette structures (D14-D16). Rosette-stage cultures were passaged
944 manually 1:1 onto poly-d-lysine (PDL) and laminin-coated tissue culture plates and grown to
945 confluence. Cells were cultured until d23 and passaged enzymatically with Accutase (Invitrogen)
946 onto PDL and laminin-coated substrates at 1.9x10^4 cells/cm^2- 2.2x10^4 cells/cm^2. At d25,
947 cultures were switched to Neural Differentiation medium (NDM) (Neurobasal medium (Gibco),
948 2% B27 (Gibco), 1% non-essential amino acids (NEAA; Gibco), 1% Penicillin-Streptomycin (Gibco)
949 2mM Glutamax (Gibco) 10 ng/ml brain-derived neurotrophic factor (BDNF; Peprotech), 10ng/ml
950 glial-derived neurotrophic factor (GDNF, Peprotech), 1 µM cyclic AMP (cAMP, Sigma), and 200
951 µM ascorbic acid (AA, Sigma). Cells were cultured in NDM until assay endpoint. For DAPT-treated
952 cultures, DAPT (Tocris Bioscience) was added for 5 days at 10 µM. For EdU labeling, Edu was
953 added at 5 µM for 24 hours, and detected using the Click-iT EdU Imaging Kit (Invitrogen).

954 Doxycycline (1 µM) was added to EdU-labeled, pDAPT cultures at the time of EdU
955 addition/labeling.
956 For longitudinal imaging of forebrain cortical neurons and interneurons, euploid (198-1)
957 and T21 (198-5) hiPSCs were maintained on Matrigel coated plates in mTESR media before
958 differentiation. Forebrain cortical neurons were derived from hiPSCs as described in [86]. Briefly,
959 neural differentiation was induced with Smad inhibitors Dorsomorphin (1.5 µM) and SB431542
960 (10 µM) for 11 days. Inhibitors were removed on day 12, and supplemented with retinoic acid
961 (0.05 µM) on day 16. At day 20, cells were dissociated with 0.05% trypsin-EDTA, resuspended in
962 media with BDNF (2ng/mL), GDNF (2ng/mL) and retinoic acid (0.05 µM) and plated 1:2 onto Poly-
963 L-ornithine-Laminin coated dish. For forebrain interneuron differentiation, hiPSCs were first
964 dissociated as colonies with CollagenaseIV/Dispase (1mg/mL each; Invitrogen) and further into
965 single cells using 0.05% trypsin-EDTA. Then, 10,000 cells were plated on low attachment round
966 bottom 96-well plate to form suspension embryoid bodies (sEB) in optimized B27 + 5 factor
967 (B27+5F) media (as described in [87]). On day 7, sEBs (35–40 per well) were transferred to 6-well
968 Matrigel coated plates, without ROCK inhibitor. On day 14, media was replaced with the addition
969 of Purmorphamine (1µM) only. On day 25, adherent embryoid bodies (aEB) were dissociated
970 using 0.05% trypsin-EDTA, passed through 70 µm cell-strainer, and plated at a density of 10,000-
971 25,000 cells/cm^2 onto Poly-L-ornithine-Laminin coated plates. Neurons were matured in B27
972 media containing DAPT (10 µM) and BDNF (2ng/mL). The pHR-hSyn1-RGEDI-P2a-EGFP lentivirus
973 (MOI=1) was added to forebrain cortical neurons (Day 35) and interneurons (Day 56) for survival
974 analysis as described [57] and imaged with robotic microscopy [88] every 12 hours for 10 days. The
975 cells were maintained in an environmental chamber with 5% CO_2 during imaging. These live cell
976 images were taken on an inverted microscope (Nikon Ti-E) at 20X magnification. A customized
977 software controlling Micromanager (version 2.0 gamma) is used to allow the automated runs
978 return to the same field of view on the plate for longitudinal imaging in 3D space.
979
980 **Single-nuclei RNA sequencing**
981 Neural cultures were treated with TrypLE (Life Technologies) for 4 minutes at 37C, and
982 cells counted with Trypan blue on the Countess Automated Cell Counter. Nuclei isolation was

983 performed with the Nuclei Isolation Kit: Nuclei EZ Prep (Sigma-Aldrich) with some modifications.
984 Briefly, cells were centrifuged at 1330 rpm for 3.5 minutes, media aspirated, and resuspended in
985 Nuclei PURE Lysis Buffer containing 1M DTT, 10% Triton X-100 and RNAsin. Nuclei were
986 centrifuged at 500g and 4C for 5 minutes in a swing-bucket rotor centrifuge, and lysis buffer was
987 aspirated. Nuclei resuspended in Nuclei PURE Sucrose Cushion buffer and RNAsin were pelleted
988 at 500g and 4C for 5 minutes, resuspended again in 25% iodixanol solution (0.28 ml of Nuclei
989 PURE Sucrose Cushion buffer containing RNAsin + 0.2 ml of 60% iodixanol), and under-layered by
990 corresponding 30% and 35% iodixanol solutions. Nuclei traverse the 25% and 30% layers of this
991 density gradient upon centrifugation (3166g at 4C for 30 minutes), and were collected from the
992 30% to 35% interface in volume of 0.3 ml. Resuspended in PURE Storage Buffer (1 ml) and (5 µl)
993 of RNAsin, nuclei were pelleted at 3166g for 15 minutes at 4C, resuspended in remaining 0.1 ml,
994 and counted again. Isolated nuclei were stored at -80 until fixation. Nuclei fixation was performed
995 according to the Evercode Fixation v2 protocol (Parse Biosciences). Nuclei were counted after
996 fixation and barcoded using the Evercode WT mini v2, following the manufacturer's instructions.
997 Sublibraries were quantified using the Agilent Tapestation, pooled in proportion to their
998 respective nuclei counts, and sequenced on MiSeq v2 and NextSeq 550 v2.5 mid-output kits
999 (Illumina).
1000
1001 **Animals**
1002 Ts(1716)65Dn (Ts65Dn; strain #005252) mice were obtained through crossings of a
1003 B6EiC3Sn a/A-Ts (1716)65Dn (Ts65Dn) female to F1 hybrid B6C3F1/J males purchased from The
1004 Jackson Laboratory. Genotyping was performed by amplifying genomic DNA with an in-house
1005 protocol. The colony of Ts65Dn mice was maintained in the Animal Facilities in the Barcelona
1006 Biomedical Research Park (PRBB, Barcelona, Spain). Mice received chow and water ad libitum in
1007 controlled laboratory conditions with temperature maintained at 22 ± 1oC and humidity at 55 ±
1008 10% on a 12h light/dark cycle (lights off 20:00h). The control group consisted of wild-type (WT)
1009 euploid littermates. All experimental procedures were approved by the local ethical committee
1010 (Comité Ético de Experimentación Animal del PRBB (CEEA-PRBB); procedure number MDS-12-
1011 1464P3), and met the guidelines of the local (law 32/2007) and European regulations (EU

1012 directive n° 86/609, EU decree 2001-486) and the Standards for the use of Laboratory Animals n°
1013 A5388-01 (NIH).
1014
1015 **Slice immunohistochemistry**
1016 Breeding pairs were established so that vaginal plugs could be checked twice daily. The
1017 presence of a vaginal plug was designated as E0.5. A 10% weight gain at E10 was used to confirm
1018 pregnancy. Male and female embryos were collected from pregnant trisomic dams at E18.5,
1019 chilled, decapitated immediately and processed for fluorescent immunohistochemical staining.
1020 Fetal heads were immersed in Paraformaldehyde 4% (PFA) (Sigma Aldrich) and the brain was
1021 dissected 24 hours later and immersed again in PFA o/n. Brains were cryoprotected by immersion
1022 in 30% sucrose solution and embedded in OCT for posterior histological processing. Embryos
1023 heads were embedded in optimal cutting temperature compound (OCT) and embedded tissue
1024 was frozen rapidly and either stored at − 80 °C or immediately sectioned into 20-µm thick frozen
1025 sections using a cryostat (Leica CM3050S). Histological sections were placed in Superfrost® slides
1026 and placed at -20ºC. We processed two sections at three different coordinates (+1.81/2.52/3.15
1027 from Bregma). Slices were fixed with methanol and incubated with blocking buffer (Tris-Buffered
1028 Saline, TBS, with 0,5% Triton-X 100 and 6% normal donkey serum). Primary antibodies were
1029 diluted in TBS ++ (TBS with 0,1% Triton-X 100 and 6% normal donkey serum): anti-S100b (Rabbit,
1030 1:1000; Synaptic systems, #287003) and anti-Ki67 (Rabbit, 1:500; Abcam, ab15580). Slices were
1031 incubated with primary antibodies overnight. After three washes with TBS, sections were
1032 incubated with the following secondary antibodies diluted in TBS ++: goat anti-rabbit (1:500;
1033 Alexa 594, Invitrogen A11012) and goat anti-rabbit (1:500; Alexa 488, A-11008) . Slices were
1034 washed with TBS three times and incubated ten minutes with Hoechst 33342. Finally, sections
1035 were mounted on glass slides using an aqueous mounting media, Mowiol. To quantify the density
1036 of S100B cells six sections per animal were imaged using a Leica TCS SP5 inverted scanning laser
1037 microscope (Leica Microsystems). 15 - 16-µm thick z-stacks (512 x 512 resolution, 8 bits) of each
1038 region of interest (ROI) in the cortex of embryos, were acquired using a 20X objective (N.A = 0.8).
1039
1040

1041 **STATISTICAL ANALYSIS**

1042 ***Image analysis***

1043 For IF (H3K27me3 and H2AK119ub) and *XIST* FISH in hiPSCs, automated image
1044 quantification relative to all Hoechst33342 labeled cells was performed using a custom
1045 CellProfiler pipeline [89], which was run in 2 phases. First, images were optimized for computer
1046 recognition using the following CellProfiler functions on each channel of each image:
1047 RescaleIntensity, CorrectIlluminationCalculate, CorrectIlluminationApply, and ReduceNoise.
1048 Then signals for nuclei, IF, and *XIST* FISH were quantified using the IdentifyPrimaryObjects
1049 functions, and counts for IF or *XIST*-positive nuclei were obtained using RelateObjects and
1050 FilterObjects. Images were output alongside outline annotations for objects recognized by
1051 CellProfiler to visually verify accuracy and consistency of automated counts. For EdU and *XIST*
1052 FISH, as well as IF of hiPSC-derived neural lineages (MAP2, S100B), images were imported and
1053 labeled cells counted manually using ImageJ (NIH, Bethesda). Differences in median fraction of
1054 labeled cells were assessed by two-tailed Wilcoxon rank-sum test.

1055 For longitudinal imaging of forebrain cortical neurons and interneurons, images were
1056 segmented using EGFP morphology, background subtracted, aligned together across timepoints,
1057 and then extracted channel intensity and feature information from each neuron into a csv file.
1058 Survival analysis was performed by defining the time of death as the point at which the GEDI ratio
1059 (RGEDI signal: EGFP expression) of a longitudinally imaged neuron exceeds the empirically
1060 calculated GEDI threshold [57]. Additionally, single cells were tracked [58] and cumulative death was
1061 calculated using Linear mixed model with Holm correction in R studio (version 4. 0. 4).

1062 For slice immunochemistry images, labeled cells were manually counted using ImageJ
1063 (NIH, Bethesda). Cell counting was performed using the Cell Counter plugin on ImageJ in a
1064 maximum projection of all z-stacks (1 µm step size). Cell counts from the cortex were processed
1065 first by image, then by coordinate (two images were taken from each coordinate), then by animal
1066 and finally by genotype. To quantify the density of Ki67 cells three sections per animal were
1067 imaged in the same form than S100B but imaging the ventricular zone of the cortex, the area
1068 with higher proliferation. An area of 100 μm^2 was delimited to normalize across sections and due
1069 to the high density of cells in this area. Outliers in data sets from both euploid and trisomic mice

1070 were statistically determined using a calculation of interquartile range (IQR). All data points
1071 outside of the IQR fences were excluded from analysis without bias. All variables were assessed
1072 with a two-tailed, independent samples Student's t test, and passed both the Shapiro-Wilks
1073 normality test and an equal variance test.
1074
1075 ***Expression and DNA methylation analysis***
1076 FASTQ files were quality controlled using FASTQC, reads were filtered and adapter-
1077 trimmed was done using BBDuk [90]. Expression quantification was performed using Salmon [91], and
1078 differential expression analysis was performed using DESeq2 [92]. Gene set enrichments were
1079 performed using the GSEA function from the R package clusterProfiler [93] on the following gene
1080 sets: Biocarta, GO (Biological Processes, Cellular Components, and Molecular Functions), KEGG,
1081 Pathway Interaction Database, Reactome, and WikiPathways. For DNAme analysis, the
1082 MethylEPIC IDAT files were processed using the R package minfi and its preprocessIllumina
1083 function to obtain methylation β-values [94]. Promoter probes were defined as having one of the
1084 following designations in the array manifest file: TSS1500, TSS200, or 5_UTR.
1085
1086 ***Phased allelic RNA-seq analysis***
1087 The 10X Genomics Long Ranger pipeline was used to align reads, and call and phase SNPs,
1088 indels, and structural variants from linked-read WGS reads. The processed FASTQs from above
1089 were aligned using HISAT2 to the hg38 human reference genome [95]. Relevant chr21 SNPs were
1090 extracted from the Long Ranger output and used to get haplotype gene expression counts from
1091 aligned RNA-seq bam files using the phASER software package [96]. While this provided reliable
1092 intragenic phasing, for intergenic phasing on chr21 we relied on the imbalanced haplotype gene
1093 expression in the T21, compared to its isogenic euploid controls. The higher expressed haplotype
1094 was designated as the major (duplicated or $chr21^{M/M2}$) haplotype and the other as the minor
1095 haplotype ($chr21^{P}$).
1096
1097
1098

1099 ***Single-nuclei RNA-seq analysis***

1100 FASTQ files were processed using the split-pipe pipeline (Parse Biosciences), and
1101 imported to Seurat [97]. We excluded nuclei with over 10% reads mapping to the mitochondrial
1102 genome, fewer than 2500 mapped reads, fewer than 1500 genes detected, or over 7500 genes
1103 detected. Following normalization and cell cycle scoring, the data were SC-transformed [62] while
1104 regressing out the mitochondrial read fraction, and samples integrated. UMAPs were projected
1105 using the first 30 principal components, and clusters labeled under default settings. Cell types
1106 were identified and grouped using markers from [60] and sctype [61]. Allelic counts from single nuclei
1107 were phased as described above, and aggregated across all chr21 genes to mitigate the impact
1108 of transcriptional bursts. Chr21 dosage by cell (aggregating across chr21 genes), or by gene
1109 (aggregating across cells) was performed on counts-per-million (cpm) normalized expression.
1110 Differences in median LAF or chr21 dosage ratio were assessed by two-tailed Wilcoxon rank-sum
1111 test, and differences in distribution by two-sample Kolmogorov-Smirnov test.

1112 For differential expression analysis, Seurat functions PrepSCTFindMarkers and
1113 FindMarkers using the ROC (receiver operating characteristic curve) test were applied to
1114 compare euploid, *XIST*$^{+}$ d0 and pD cells to *XIST*-negative T21 cells by cell type group. GSEA was
1115 performed as for bulk RNA-seq while limiting gene terms to Hallmark and canonical pathways
1116 (KEGG, Reactome, wikipathways, PID, biocarta) of MSigDB.

1117
1118
1119
1120
1121
1122
1123
1124
1125
1126
1127

ACKNOWLEDGEMENTS

This work was supported by grants from the LuMind IDSC Foundation and the NIH (R35GM124926, with additional support from R01HL141324) to S.F.P . We are grateful to Gordon Carmichael and James Li for helpful comments on our manuscript. We also thank the University of Connecticut's Cell and Genome Engineering Core and Center for Genome Innovation for reprogramming, as well as mRNA-seq, CytoSNP, linked-read WGS and methylEPIC core services, respectively. Support for work conducted at the Gladstone institutes (S.F.) came from R01AG064579 with additional support from R01LM013617, RF1NS128800 and the JSRM Foundation. Work at the Centre for Genomic Regulation (M.D.) was supported by the Fondation Jérôme Lejeune #2002, Fundació La Marató De TV3 202212-30-31-32, and Agencia Estatal de Investigación (PID2019- 110755RB-I00/AEI / 10.13039/501100011033). We acknowledge support of the Spanish Ministry of Science and Innovation to the EMBL partnership, the Centro de Excelencia Severo Ochoa and the CERCA Programme / Generalitat de Catalunya, and the FPU fellowship (FPU19/04789) from Ministerio de Universidades (to M.S.N.) The CIBER of Rare Diseases is an initiative of the ISCIII.

DECLARATION OF INTERESTS

No competing interests

1157 **REFERENCES**

1158 1. Capone, G. T., Chicoine, B., Bulova, P., Stephens, M., Hart, S., Crissman, B., *et al.* Co-
1159 occurring medical conditions in adults with Down syndrome: A systematic review toward
1160 the development of health care guidelines. *Am. J. Med. Genet. Part A* **176**, 116–133
1161 (2018).
1162 2. Antonarakis, S. E., Skotko, B. G., Rafii, M. S., Strydom, A., Pape, S. E., Bianchi, D. W., *et al.*
1163 Down syndrome. *Nat. Rev. Dis. Prim.* **6**, 1–20 (2020).
1164 3. Kazuki, Y., Gao, F. J., Li, Y., Moyer, A. J., Devenney, B., Hiramatsu, K., *et al.* A non-mosaic
1165 transchromosomic mouse model of down syndrome carrying the long arm of human
1166 chromosome 21. *Elife* **9**, 1–29 (2020).
1167 4. Kazuki, Y., Gao, F. J., Yamakawa, M., Hirabayashi, M., Kazuki, K., Kajitani, N., *et al.* A
1168 transchromosomic rat model with human chromosome 21 shows robust Down syndrome
1169 features. *Am. J. Hum. Genet.* **109**, 328–344 (2022).
1170 5. Herault, Y., Delabar, J. M., Fisher, E. M. C., Tybulewicz, V. L. J., Yu, E. & Brault, V. Rodent
1171 models in Down syndrome research: impact and future opportunities. *Dis. Model. Mech.*
1172 **10**, 1165–1186 (2017).
1173 6. Bhattacharyya, A. Advancing knowledge of down syndrome brain development and
1174 function with human stem cells. *Am. J. Intellect. Dev. Disabil.* **25**, 90–92 (2020).
1175 7. Suzuki, I. K. & Vanderhaeghen, P. Is this a brain which i see before me? Modeling human
1176 neural development with pluripotent stem cells. *Development (Cambridge)* vol. 142
1177 3138–3150 (2015).
1178 8. van den Ameele, J., Tiberi, L., Vanderhaeghen, P. & Espuny-Camacho, I. Thinking out of
1179 the dish: what to learn about cortical development using pluripotent stem cells. *Trends*
1180 *Neurosci.* **37**, 334–42 (2014).
1181 9. Cookson, M. R. Evolution of Neurodegeneration. *Curr. Biol.* **22**, R753–R761 (2012).
1182 10. Shabani, K. & Hassan, B. A. The brain on time: Links between development and
1183 neurodegeneration. *Dev.* **150**, (2023).
1184 11. Altafaj, X., Martín, E. D., Ortiz-Abalia, J., Valderrama, A., Lao-Peregrín, C., Dierssen, M., *et*
1185 *al.* Normalization of Dyrk1A expression by AAV2/1-shDyrk1A attenuates hippocampal-
1186 dependent defects in the Ts65Dn mouse model of Down syndrome. *Neurobiol. Dis.* **52**,
1187 117–127 (2013).
1188 12. Wiseman, F. K., Al-Janabi, T., Hardy, J., Karmiloff-Smith, A., Nizetic, D., Tybulewicz, V. L. J.,
1189 *et al.* A genetic cause of Alzheimer disease: Mechanistic insights from Down syndrome.
1190 *Nature Reviews Neuroscience* vol. 16 564–574 (2015).
1191 13. Rosi, S. & Frias, E. S. The Integrated Stress Response: A Central Memory Switch in Down
1192 Syndrome. *Cell Metab.* **31**, 15–17 (2020).
1193 14. Zhu, P. J., Khatiwada, S., Cui, Y., Reineke, L. C., Dooling, S. W., Kim, J. J., *et al.* Activation of
1194 the ISR mediates the behavioral and neurophysiological abnormalities in down
1195 syndrome. *Science (80-.).* **366**, 843–849 (2019).
1196 15. Tramutola, A., Lanzillotta, C., Arena, A., Barone, E., Perluigi, M. & Di Domenico, F.
1197 Increased Mammalian Target of Rapamycin Signaling Contributes to the Accumulation of
1198 Protein Oxidative Damage in a Mouse Model of Down's Syndrome. *Neurodegener. Dis.*
1199 **16**, 62–68 (2016).

1200 16. Zamponi, E., Zamponi, N., Coskun, P., Quassollo, G., Lorenzo, A., Cannas, S. A., *et al.* Nrf2
1201 stabilization prevents critical oxidative damage in Down syndrome cells. *Aging Cell* **17**,
1202 e12812 (2018).
1203 17. Helguera, P., Pelsman, A., Pigino, G., Wolvetang, E., Head, E. & Busciglio, J. ets-2
1204 promotes the activation of a mitochondrial death pathway in Down's syndrome neurons.
1205 *J. Neurosci.* **25**, 2295–303 (2005).
1206 18. Helguera, P., Seiglie, J., Rodriguez, J., Hanna, M., Helguera, G. & Busciglio, J. Adaptive
1207 downregulation of mitochondrial function in down syndrome. *Cell Metab.* **17**, 132–40
1208 (2013).
1209 19. Di Domenico, F., Coccia, R., Cocciolo, A., Murphy, M. P., Cenini, G., Head, E., *et al.*
1210 Impairment of proteostasis network in Down syndrome prior to the development of
1211 Alzheimer's disease neuropathology: Redox proteomics analysis of human brain.
1212 *Biochim. Biophys. Acta - Mol. Basis Dis.* **1832**, 1249–1259 (2013).
1213 20. Hwang, S., Cavaliere, P., Li, R., Zhu, L. J., Dephoure, N. & Torres, E. M. Consequences of
1214 aneuploidy in human fibroblasts with trisomy 21. *Proc. Natl. Acad. Sci.* **118**, e2014723118
1215 (2021).
1216 21. Jiang, J., Jing, Y., Cost, G. J., Chiang, J.-C., Kolpa, H. J., Cotton, A. M., *et al.* Translating
1217 dosage compensation to trisomy 21. *Nature* **500**, 296–300 (2013).
1218 22. Pinter, S. F. A Tale of Two Cities: How Xist and its partners localize to and silence the
1219 bicompartmental X. *Semin. Cell Dev. Biol.* **56**, 19–34 (2016).
1220 23. Wutz, A. & Jaenisch, R. A shift from reversible to irreversible X inactivation is triggered
1221 during ES cell differentiation. *Mol. Cell* **5**, 695–705 (2000).
1222 24. Kohlmaier, A., Savarese, F., Lachner, M., Martens, J., Jenuwein, T. & Wutz, A. A
1223 chromosomal memory triggered by Xist regulates histone methylation in X inactivation.
1224 *PLoS Biol* **2**, E171 (2004).
1225 25. Savarese, F., Flahndorfer, K., Jaenisch, R., Busslinger, M. & Wutz, A. Hematopoietic
1226 precursor cells transiently reestablish permissiveness for X inactivation. *Mol. Cell. Biol.*
1227 **26**, 7167–77 (2006).
1228 26. Agrelo, R., Souabni, A., Novatchkova, M., Haslinger, C., Leeb, M., Komnenovic, V., *et al.*
1229 SATB1 defines the developmental context for gene silencing by Xist in lymphoma and
1230 embryonic cells. *Dev. Cell* **16**, 507–516 (2009).
1231 27. Czermiński, J. T. & Lawrence, J. B. Silencing Trisomy 21 with XIST in Neural Stem Cells
1232 Promotes Neuronal Differentiation. *Dev. Cell* (2020) doi:10.1016/j.devcel.2019.12.015.
1233 28. Guidi, S., Bonasoni, P., Ceccarelli, C., Santini, D., Gualtieri, F., Ciani, E., *et al.* Neurogenesis
1234 impairment and increased cell death reduce total neuron number in the hippocampal
1235 region of fetuses with Down syndrome. *Brain Pathol.* **18**, 180–197 (2008).
1236 29. Zdaniuk, G., Wierzba-Bobrowicz, T., Szpak, G. M. & Stępień, T. Astroglia disturbances
1237 during development of the central nervous system in fetuses with Down's syndrome.
1238 *Folia Neuropathol.* **49**, 109–114 (2011).
1239 30. Lu, J., Esposito, G., Scuderi, C., Steardo, L., Delli-Bovi, L. C., Hecht, J. L., *et al.* S100B and
1240 APP promote a gliocentric shift and impaired neurogenesis in down syndrome neural
1241 progenitors. *PLoS One* **6**, (2011).
1242 31. Lu, J., Lian, G., Zhou, H., Esposito, G., Steardo, L., Delli-Bovi, L. C., *et al.* OLIG2 over-
1243 expression impairs proliferation of human Down syndrome neural progenitors. *Hum.*

1244 *Mol. Genet.* **21**, 2330–2340 (2012).
1245 32. Guidi, S., Giacomini, A., Stagni, F., Emili, M., Uguagliati, B., Bonasoni, M. P., *et al.*
1246 Abnormal development of the inferior temporal region in fetuses with Down syndrome.
1247 *Brain Pathol.* **28**, 986–998 (2018).
1248 33. Holtzman, D. M., Santucci, D., Kilbridge, J., Chua-Couzens, J., Fontana, D. J., Daniels, S. E.,
1249 *et al.* Developmental abnormalities and age-related neurodegeneration in a mouse
1250 model of Down syndrome. *Proc. Natl. Acad. Sci. U. S. A.* **93**, 13333–13338 (1996).
1251 34. Kurabayashi, N., Nguyen, M. D. & Sanada, K. DYRK1A overexpression enhances STAT
1252 activity and astrogliogenesis in a Down syndrome mouse model. *EMBO Rep.* **16**, 1548–
1253 1562 (2015).
1254 35. Stagni, F., Giacomini, A., Emili, M., Uguagliati, B., Bonasoni, M. P., Bartesaghi, R., *et al.*
1255 Subicular hypotrophy in fetuses with Down syndrome and in the Ts65Dn model of Down
1256 syndrome. *Brain Pathol.* **29**, 366–379 (2019).
1257 36. Lubiniecki, A. S., Blattner, W. A., Martin, G. M., Fialkow, P. J., Dosik, H., Eatherly, C., *et al.*
1258 SV40 T-antigen expression in cultured fibroblasts from patients with Down syndrome and
1259 their parents. *Am. J. Hum. Genet.* **31**, 469–477 (1979).
1260 37. Laurent, L. C., Ulitsky, I., Slavin, I., Tran, H., Schork, A., Morey, R., *et al.* Dynamic changes
1261 in the copy number of pluripotency and cell proliferation genes in human ESCs and iPSCs
1262 during reprogramming and time in culture. *Cell Stem Cell* **8**, 106–118 (2011).
1263 38. Taapken, S. M., Nisler, B. S., Newton, M. A., Sampsell-Barron, T. L., Leonhard, K. A.,
1264 McIntire, E. M., *et al. Karotypic abnormalities in human induced pluripotent stem cells*
1265 *and embryonic stem cells*. *Nature Biotechnology* vol. 29 313–314 (2011).
1266 39. Papavassiliou, P., Charalsawadi, C., Rafferty, K. & Jackson-Cook, C. Mosaicism for trisomy
1267 21: A review. *Am. J. Med. Genet. Part A* **167**, 26–39 (2015).
1268 40. Weick, J. P., Held, D. L., Bonadurer, G. F., Doers, M. E., Liu, Y., Maguire, C., *et al.* Deficits
1269 in human trisomy 21 iPSCs and neurons. *Proc. Natl. Acad. Sci. U. S. A.* **110**, 9962–7
1270 (2013).
1271 41. Hibaoui, Y., Grad, I., Letourneau, A., Sailani, M. R., Dahoun, S., Santoni, F. A., *et al.*
1272 Modelling and rescuing neurodevelopmental defect of Down syndrome using induced
1273 pluripotent stem cells from monozygotic twins discordant for trisomy 21. *EMBO Mol.*
1274 *Med.* **6**, 259–77 (2014).
1275 42. Murray, A., Letourneau, A., Canzonetta, C., Stathaki, E., Gimelli, S., Sloan-Bena, F., *et al.*
1276 Brief Report: Isogenic Induced Pluripotent Stem Cell Lines From an Adult With Mosaic
1277 Down Syndrome Model Accelerated Neuronal Ageing and Neurodegeneration. *Stem Cells*
1278 **33**, 2077–2084 (2015).
1279 43. MacLean, G. A., Menne, T. F., Guo, G., Sanchez, D. J., Park, I.-H., Daley, G. Q., *et al.*
1280 Altered hematopoiesis in trisomy 21 as revealed through in vitro differentiation of
1281 isogenic human pluripotent cells. *Proc. Natl. Acad. Sci.* **109**, 17567–17572 (2012).
1282 44. Inoue, M., Kajiwara, K., Yamaguchi, A., Kiyono, T., Samura, O., Akutsu, H., *et al.*
1283 Autonomous trisomic rescue of Down syndrome cells. *Lab. Investig.* **99**, 885–897 (2019).
1284 45. Csankovszki, G., Panning, B., Bates, B., Pehrson, J. R. & Jaenisch, R. Conditional deletion
1285 of Xist disrupts histone macroH2A localization but not maintenance of X inactivation.
1286 *Nat. Genet.* **22**, 323–324 (1999).
1287 46. Csankovszki, G., Nagy, A. & Jaenisch, R. Synergism of Xist Rna, DNA Methylation, and

1288 Histone Hypoacetylation in Maintaining X Chromosome Inactivation. *J. Cell Biol.* **153**,
1289 773–784 (2001).
1290 47. Moullan, N., Mouchiroud, L., Wang, X., Ryu, D., Williams, E. G., Mottis, A., *et al.*
1291 Tetracyclines disturb mitochondrial function across eukaryotic models: A call for caution
1292 in biomedical research. *Cell Rep.* **10**, 1681–1691 (2015).
1293 48. Izzo, A., Mollo, N., Nitti, M., Paladino, S., Calì, G., Genesio, R., *et al.* Mitochondrial
1294 dysfunction in down syndrome: molecular mechanisms and therapeutic targets. *Mol.*
1295 *Med.* **24**, 2 (2018).
1296 49. Valenti, D., Braidy, N., De Rasmo, D., Signorile, A., Rossi, L., Atanasov, A. G., *et al.*
1297 Mitochondria as pharmacological targets in Down syndrome. *Free Radic. Biol. Med.* **114**,
1298 69–83 (2018).
1299 50. Parra, V., Altamirano, F., Hernández-Fuentes, C. P., Tong, D., Kyrychenko, V., Rotter, D.,
1300 *et al.* Down Syndrome Critical Region 1 Gene, Rcan1, Helps Maintain a More Fused
1301 Mitochondrial Network. *Circ. Res.* **122**, e20–e33 (2018).
1302 51. Wolvetang, E. ., Bradfield, O. ., Hatzistavrou, T., Crack, P. ., Busciglio, J., Kola, I., *et al.*
1303 Overexpression of the chromosome 21 transcription factor Ets2 induces neuronal
1304 apoptosis. *Neurobiol. Dis.* **14**, 349–356 (2003).
1305 52. Hu, Y., Lehrach, H. & Janitz, M. Apoptosis screening of human chromosome 21 proteins
1306 reveals novel cell death regulators. *Mol. Biol. Rep.* **37**, 3381–3387 (2010).
1307 53. Noll, C., Tlili, A., Ripoll, C., Mallet, L., Paul, J. L., Delabar, J. M., *et al.* Dyrk1a activates
1308 antioxidant NQO1 expression through an ERK1/2-Nrf2 dependent mechanism. *Mol.*
1309 *Genet. Metab.* **105**, 484–488 (2012).
1310 54. Liu, Y., Borel, C., Li, L., Müller, T., Williams, E. G., Germain, P. L., *et al.* Systematic
1311 proteome and proteostasis profiling in human Trisomy 21 fibroblast cells. *Nat. Commun.*
1312 *2017 81* **8**, 1–15 (2017).
1313 55. Banda, E. & Grabel, L. Directed Differentiation of Human Embryonic Stem Cells into
1314 Neural Progenitors. in *Methods in molecular biology (Clifton, N.J.)* vol. 1307 289–298
1315 (2014).
1316 56. Banda, E., McKinsey, A., Germain, N., Carter, J., Anderson, N. C. & Grabel, L. Cell Polarity
1317 and Neurogenesis in Embryonic Stem Cell-Derived Neural Rosettes. *Stem Cells Dev.* **24**,
1318 1022–1033 (2015).
1319 57. Linsley, J. W., Shah, K., Castello, N., Chan, M., Haddad, D., Doric, Z., *et al.* Genetically
1320 encoded cell-death indicators (GEDI) to detect an early irreversible commitment to
1321 neurodegeneration. *Nat. Commun.* **12**, 1–14 (2021).
1322 58. Chang, Y. H., Linsley, J., Lamstein, J., Kalra, J., Epstein, I., Barch, M., *et al.* Single cell
1323 tracking based on Voronoi partition via stable matching. *Proc. IEEE Conf. Decis. Control*
1324 **2020**-**Decem**, 5086–5091 (2020).
1325 59. Molofsky, A. V., Krencick, R., Ullian, E. M., Tsai, H. -h., Deneen, B., Richardson, W. D., *et*
1326 *al.* Astrocytes and disease: a neurodevelopmental perspective. *Genes Dev.* **26**, 891–907
1327 (2012).
1328 60. Burke, E. E., Chenoweth, J. G., Shin, J. H., Collado-Torres, L., Kim, S.-K., Micali, N., *et al.*
1329 Dissecting transcriptomic signatures of neuronal differentiation and maturation using
1330 iPSCs. *Nat. Commun.* **11**, 462 (2020).
1331 61. Ianevski, A., Giri, A. K. & Aittokallio, T. Fully-automated and ultra-fast cell-type

1332 identification using specific marker combinations from single-cell transcriptomic data.
1333 *Nat. Commun. 2022 131* **13**, 1–10 (2022).
1334 62. Hafemeister, C. & Satija, R. Normalization and variance stabilization of single-cell RNA-
1335 seq data using regularized negative binomial regression. *Genome Biol.* **20**, 1–15 (2019).
1336 63. Tobe, R., Naranjo-Suarez, S., Everley, R. A., Carlson, B. A., Turanov, A. A., Tsuji, P. A., *et al.*
1337 High Error Rates in Selenocysteine Insertion in Mammalian Cells Treated with the
1338 Antibiotic Doxycycline, Chloramphenicol, or Geneticin. *J. Biol. Chem.* **288**, 14709–14715
1339 (2013).
1340 64. de Toma, I., Sierra, C. & Dierssen, M. Meta-analysis of transcriptomic data reveals
1341 clusters of consistently deregulated gene and disease ontologies in Down syndrome.
1342 *PLOS Comput. Biol.* **17**, e1009317 (2021).
1343 65. Beckervordersandforth, R. Mitochondrial Metabolism-Mediated Regulation of Adult
1344 Neurogenesis. *Brain Plast.* **3**, 73–87 (2017).
1345 66. Briggs, J. A., Sun, J., Shepherd, J., Ovchinnikov, D. A., Chung, T.-L., Nayler, S. P., *et al.*
1346 Integration-Free Induced Pluripotent Stem Cells Model Genetic and Neural
1347 Developmental Features of Down Syndrome Etiology. *Stem Cells* **31**, 467–478 (2013).
1348 67. Kawatani, K., Nambara, T., Nawa, N., Yoshimatsu, H., Kusakabe, H., Hirata, K., *et al.* A
1349 human isogenic iPSC-derived cell line panel identifies major regulators of aberrant
1350 astrocyte proliferation in Down syndrome. *Commun. Biol.* **4**, 730 (2021).
1351 68. Neri, F., Rapelli, S., Krepelova, A., Incarnato, D., Parlato, C., Basile, G., *et al.* Intragenic
1352 DNA methylation prevents spurious transcription initiation. *Nat. 2017 5437643* **543**, 72–
1353 77 (2017).
1354 69. Mizuno, G. O., Wang, Y., Shi, G., Wang, Y., Sun, J., Papadopoulos, S., *et al.* Aberrant
1355 Calcium Signaling in Astrocytes Inhibits Neuronal Excitability in a Human Down Syndrome
1356 Stem Cell Model. *Cell Rep.* **24**, 355–365 (2018).
1357 70. Fernández-blanco, Á. & Dierssen, M. Rethinking Intellectual Disability from Neuro- to
1358 Astro-Pathology. *Int. J. Mol. Sci.* **21**, 1–20 (2020).
1359 71. Wang, J., Syrett, C. M., Kramer, M. C., Basu, A., Atchison, M. L. & Anguera, M. C. Unusual
1360 maintenance of X chromosome inactivation predisposes female lymphocytes for
1361 increased expression from the inactive X. *Proc. Natl. Acad. Sci.* 201520113 (2016)
1362 doi:10.1073/pnas.1520113113.
1363 72. Chiang, J. C., Jiang, J., Newburger, P. E. & Lawrence, J. B. Trisomy silencing by XIST
1364 normalizes Down syndrome cell pathogenesis demonstrated for hematopoietic defects in
1365 vitro. *Nat. Commun.* **9**, (2018).
1366 73. Rocks, D., Shukla, M., Ouldibbat, L., Finnemann, S. C., Kalluchi, A., Rowley, M. J., *et al.*
1367 Sex-specific multi-level 3D genome dynamics in the mouse brain. *Nat. Commun. 2022*
1368 *131* **13**, 1–17 (2022).
1369 74. Chow, J. C., Hall, L. L., Baldry, S. E. L., Thorogood, N. P., Lawrence, J. B. & Brown, C. J.
1370 Inducible XIST-dependent X-chromosome inactivation in human somatic cells is
1371 reversible. *Proc. Natl. Acad. Sci. U. S. A.* **104**, 10104–9 (2007).
1372 75. Kelsey, A. D., Yang, C., Leung, D., Minks, J., Dixon-McDougall, T., Baldry, S. E. L., *et al.*
1373 Impact of flanking chromosomal sequences on localization and silencing by the human
1374 non-coding RNA XIST. *Genome Biol.* **16**, 1–16 (2015).
1375 76. Loda, A., Brandsma, J. H., Vassilev, I., Servant, N., Loos, F., Amirnasr, A., *et al.* Genetic and

1376 epigenetic features direct differential efficiency of Xist-mediated silencing at X-
1377 chromosomal and autosomal locations. *Nat. Commun. 2017 81* **8**, 1–16 (2017).
1378 77. Wutz, A. Epigenetic Alterations in Human Pluripotent Stem Cells: A Tale of Two Cultures.
1379 *Cell Stem Cell* **11**, 9–15 (2012).
1380 78. Bansal, P., Ahern, D. T., Kondaveeti, Y., Qiu, C. W. & Pinter, S. F. Contiguous erosion of
1381 the inactive X in human pluripotency concludes with global DNA hypomethylation. *Cell*
1382 *Rep.* **35**, 109215 (2021).
1383 79. Lois, C., Hong, E. J., Pease, S., Brown, E. J. & Baltimore, D. Germline transmission and
1384 tissue-specific expression of transgenes delivered by lentiviral vectors. *Science* **295**, 868–
1385 872 (2002).
1386 80. DeKelver, R. C., Choi, V. M., Moehle, E. A., Paschon, D. E., Hockemeyer, D., Meijsing, S. H.,
1387 *et al.* Functional genomics, proteomics, and regulatory DNA analysis in isogenic settings
1388 using zinc finger nuclease-driven transgenesis into a safe harbor locus in the human
1389 genome. *Genome Res.* **20**, 1133–42 (2010).
1390 81. Liu, P., Jenkins, N. A. & Copeland, N. G. A Highly Efficient Recombineering-Based Method
1391 for Generating Conditional Knockout Mutations. *Genome Res.* **13**, 476–484 (2003).
1392 82. Chen, S. X., Osipovich, A. B., Ustione, A., Potter, L. A., Hipkens, S., Gangula, R., *et al.*
1393 Quantification of factors influencing fluorescent protein expression using RMCE to
1394 generate an allelic series in the ROSA26 locus in mice. *Dis. Model. Mech.* **4**, 537–547
1395 (2011).
1396 83. Zhu, Z., González, F. & Huangfu, D. The iCRISPR Platform for Rapid Genome Editing in
1397 Human Pluripotent Stem Cells. *Methods Enzymol.* **546**, 215–250 (2014).
1398 84. González, F., Zhu, Z., Shi, Z.-D., Lelli, K., Verma, N., Li, Q. V., *et al.* An iCRISPR Platform for
1399 Rapid, Multiplexable, and Inducible Genome Editing in Human Pluripotent Stem Cells.
1400 *Cell Stem Cell* **15**, 215–226 (2014).
1401 85. Ran, F. A., Hsu, P. P. D., Wright, J., Agarwala, V., Scott, D. a & Zhang, F. Genome
1402 engineering using the CRISPR-Cas9 system. *Nat. Protoc.* **8**, 2281–308 (2013).
1403 86. Burkhardt, M. F., Martinez, F. J., Wright, S., Ramos, C., Volfson, D., Mason, M., *et al.* A
1404 cellular model for sporadic ALS using patient-derived induced pluripotent stem cells. *Mol.*
1405 *Cell. Neurosci.* **56**, 355–364 (2013).
1406 87. Nicholas, C. R., Chen, J., Tang, Y., Southwell, D. G., Chalmers, N., Vogt, D., *et al.* Functional
1407 maturation of hPSC-derived forebrain interneurons requires an extended timeline and
1408 mimics human neural development. *Cell Stem Cell* **12**, 573–586 (2013).
1409 88. Arrasate, M., Mitra, S., Schweitzer, E. S., Segal, M. R. & Finkbeiner, S. Inclusion body
1410 formation reduces levels of mutant huntingtin and the risk of neuronal death. *Nature*
1411 **431**, 805–810 (2004).
1412 89. Mcquin, C., Goodman, A., Chernyshev, V., Kamentsky, L., Cimini, A., Karhohs, K. W., *et al.*
1413 Cellprofiler 3.0. *PLoS Biol.* 1–17 (2018).
1414 90. Bushnell, B. BBTools.
1415 91. Patro, R., Duggal, G., Love, M. I., Irizarry, R. A. & Kingsford, C. Salmon provides fast and
1416 bias-aware quantification of transcript expression. *Nat. Methods* **14**, 417–419 (2017).
1417 92. Love, M. I., Huber, W., Anders, S., Tusher, V., Banks, E., Fennell, T., *et al.* Moderated
1418 estimation of fold change and dispersion for RNA-seq data with DESeq2. *Genome Biol.*
1419 **15**, 550 (2014).

1420 93. Wu, T., Hu, E., Xu, S., Chen, M., Guo, P., Dai, Z., *et al.* clusterProfiler 4.0: A universal
1421 enrichment tool for interpreting omics data. *Innov.* **2**, 100141 (2021).
1422 94. Aryee, M. J., Jaffe, A. E., Corrada-Bravo, H., Ladd-Acosta, C., Feinberg, A. P., Hansen, K. D.,
1423 *et al.* Minfi: A flexible and comprehensive Bioconductor package for the analysis of
1424 Infinium DNA methylation microarrays. *Bioinformatics* **30**, 1363–1369 (2014).
1425 95. Kim, D., Paggi, J. M., Park, C., Bennett, C. & Salzberg, S. L. Graph-based genome
1426 alignment and genotyping with HISAT2 and HISAT-genotype. *Nat. Biotechnol.* **37**, 907–
1427 915 (2019).
1428 96. Castel, S. E., Mohammadi, P., Chung, W. K., Shen, Y. & Lappalainen, T. Rare variant
1429 phasing and haplotypic expression from RNA sequencing with phASER. *Nat. Commun.* **7**,
1430 1–6 (2016).
1431 97. Hao, Y., Hao, S., Andersen-Nissen, E., Mauck, W. M., Zheng, S., Butler, A., *et al.* Integrated
1432 analysis of multimodal single-cell data. *Cell* **184**, 3573-3587.e29 (2021).
1433

Figure 1

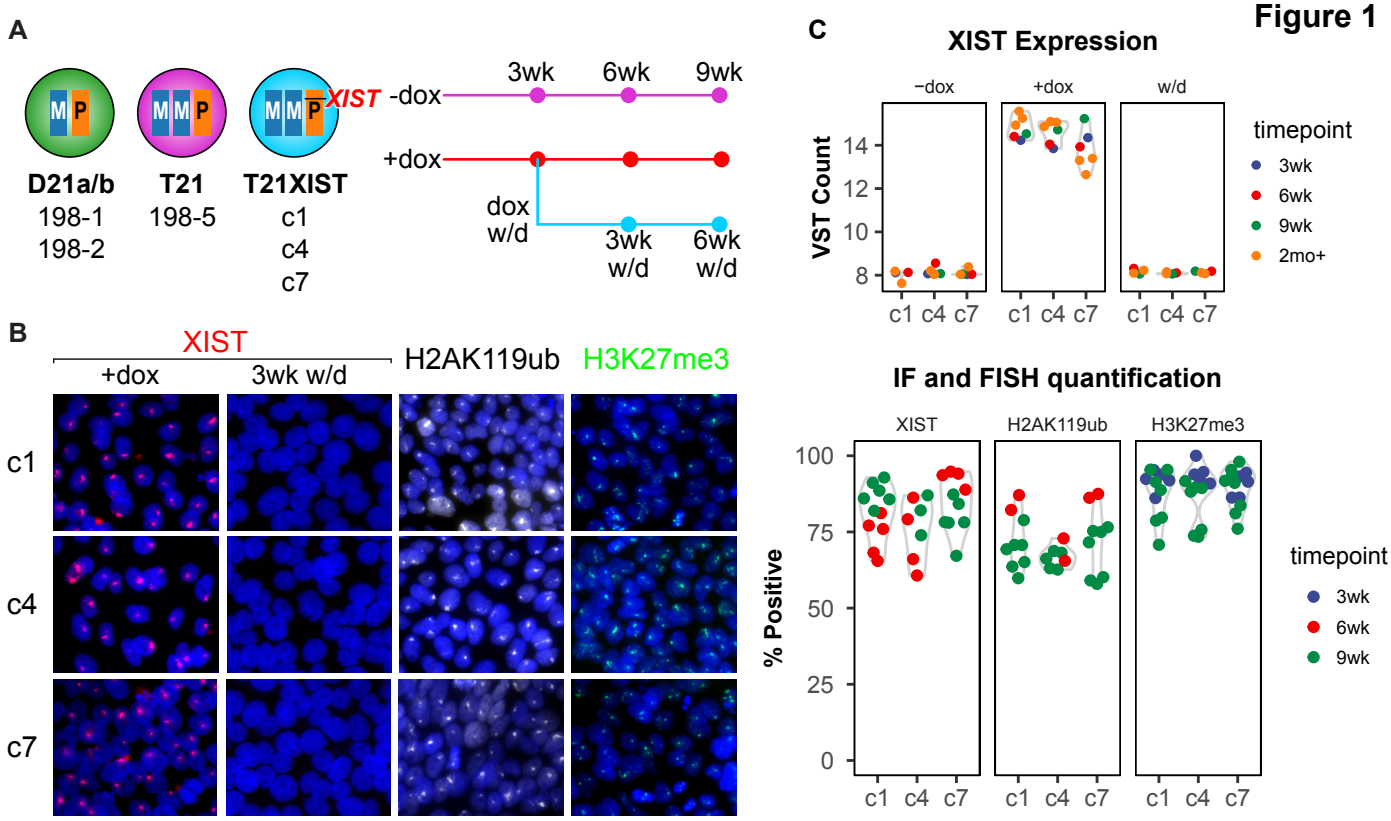
A
M P
M M P
M M P
XIST
D21a/b
198-1
198-2
T21
198-5
T21XIST
c1
c4
c7
-dox
+dox
3wk
6wk
9wk
dox
w/d
3wk
w/d
6wk
w/d
B
XIST
+dox
3wk w/d
H2AK119ub
H3K27me3
c1
c4
c7
C
XIST Expression
−dox
+dox
w/d
VST Count
14
12
10
8
c1 c4 c7
timepoint
3wk
6wk
9wk
2mo+
IF and FISH quantification
XIST
H2AK119ub
H3K27me3
% Positive
100
75
50
25
0
c1 c4 c7
timepoint
3wk
6wk
9wk

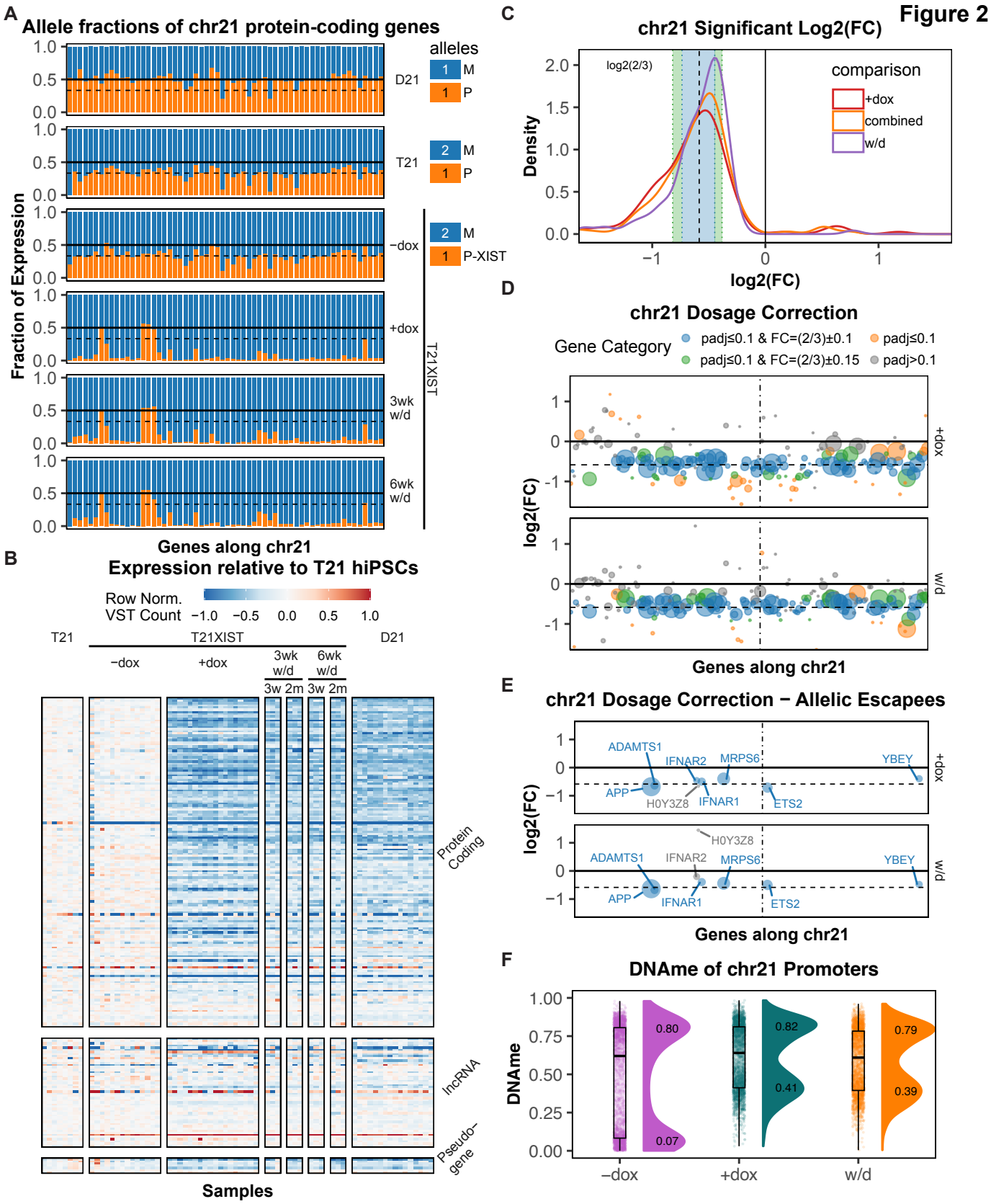
Figure 2
A
Allele fractions of chr21 protein-coding genes
alleles
D21
T21
−dox
+dox
3wk w/d
6wk w/d
M
P
P-XIST
T21XIST
Fraction of Expression
Genes along chr21
B
Expression relative to T21 hiPSCs
Row Norm. VST Count
T21
T21XIST
D21
−dox
+dox
3wk w/d
6wk w/d
3w 2m 3w 2m
Protein Coding
lncRNA
Pseudo-gene
Samples
C
chr21 Significant Log2(FC)
log2(2/3)
comparison
+dox
combined
w/d
Density
log2(FC)
D
chr21 Dosage Correction
Gene Category
padj≤0.1 & FC=(2/3)±0.1
padj≤0.1
padj≤0.1 & FC=(2/3)±0.15
padj>0.1
log2(FC)
Genes along chr21
E
chr21 Dosage Correction − Allelic Escapees
ADAMTS1
IFNAR2
MRPS6
YBEY
APP
H0Y3Z8
IFNAR1
ETS2
log2(FC)
Genes along chr21
F
DNAme of chr21 Promoters
DNAme
0.80
0.07
0.82
0.41
0.79
0.39
−dox
+dox
w/d

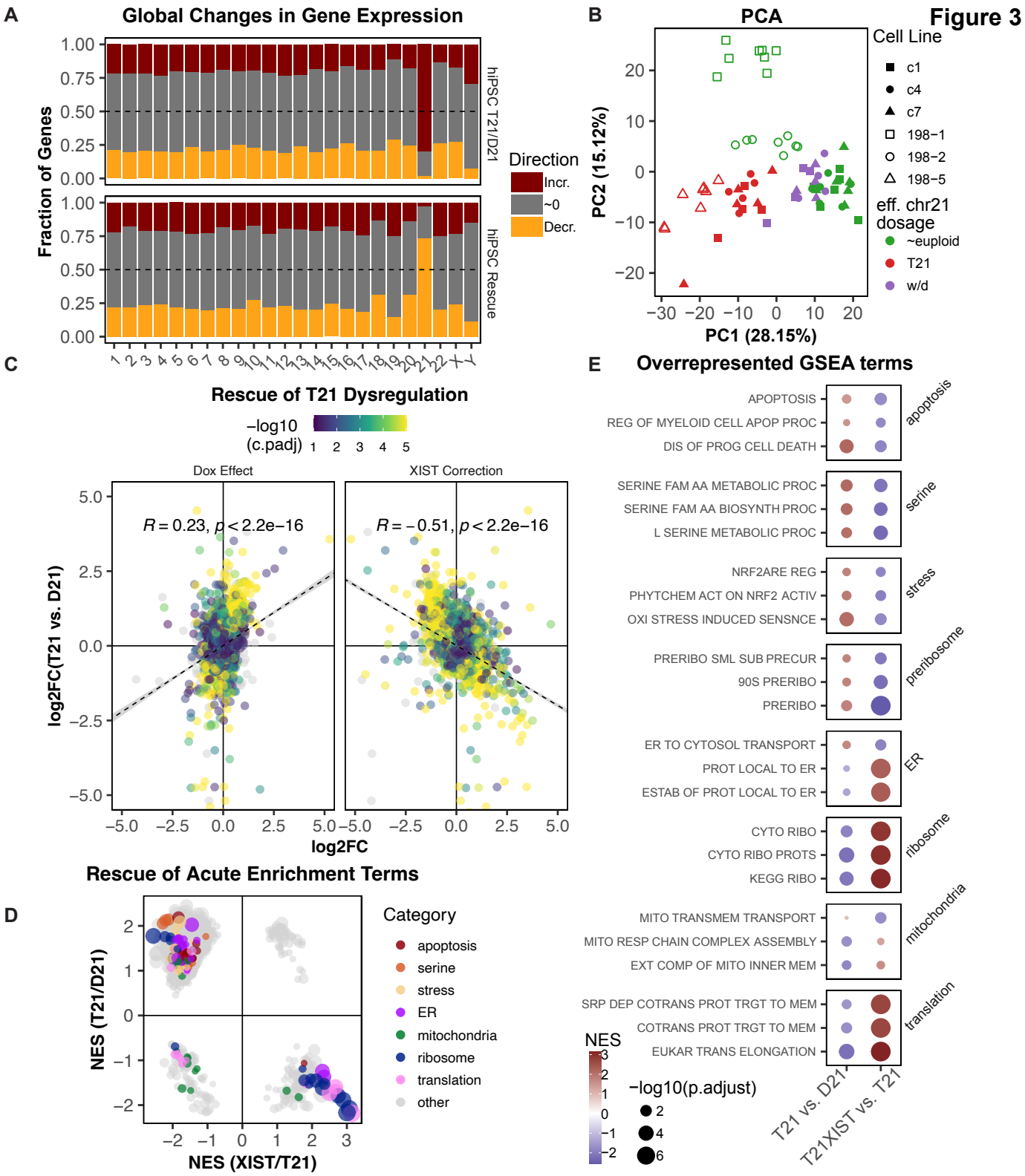
Figure 3
A
Global Changes in Gene Expression
Fraction of Genes
hiPSC T21/D21
hiPSC Rescue
Direction
Incr.
~0
Decr.
B
PCA
PC2 (15.12%)
PC1 (28.15%)
Cell Line
c1
c4
c7
198−1
198−2
198−5
eff. chr21 dosage
~euploid
T21
w/d
C
Rescue of T21 Dysregulation
−log10 (c.padj)
Dox Effect
XIST Correction
R = 0.23, p < 2.2e−16
R = −0.51, p < 2.2e−16
log2FC(T21 vs. D21)
log2FC
D
Rescue of Acute Enrichment Terms
NES (T21/D21)
NES (XIST/T21)
Category
apoptosis
serine
stress
ER
mitochondria
ribosome
translation
other
E
Overrepresented GSEA terms
APOPTOSIS
REG OF MYELOID CELL APOP PROC
DIS OF PROG CELL DEATH
apoptosis
SERINE FAM AA METABOLIC PROC
SERINE FAM AA BIOSYNTH PROC
L SERINE METABOLIC PROC
serine
NRF2ARE REG
PHYTCHEM ACT ON NRF2 ACTIV
OXI STRESS INDUCED SENSNCE
stress
PRERIBO SML SUB PRECUR
90S PRERIBO
PRERIBO
preribosome
ER TO CYTOSOL TRANSPORT
PROT LOCAL TO ER
ESTAB OF PROT LOCAL TO ER
ER
CYTO RIBO
CYTO RIBO PROTS
KEGG RIBO
ribosome
MITO TRANSMEM TRANSPORT
MITO RESP CHAIN COMPLEX ASSEMBLY
EXT COMP OF MITO INNER MEM
mitochondria
SRP DEP COTRANS PROT TRGT TO MEM
COTRANS PROT TRGT TO MEM
EUKAR TRANS ELONGATION
translation
NES
−log10(p.adjust)
T21 vs. D21
T21XIST vs. T21

Figure 4

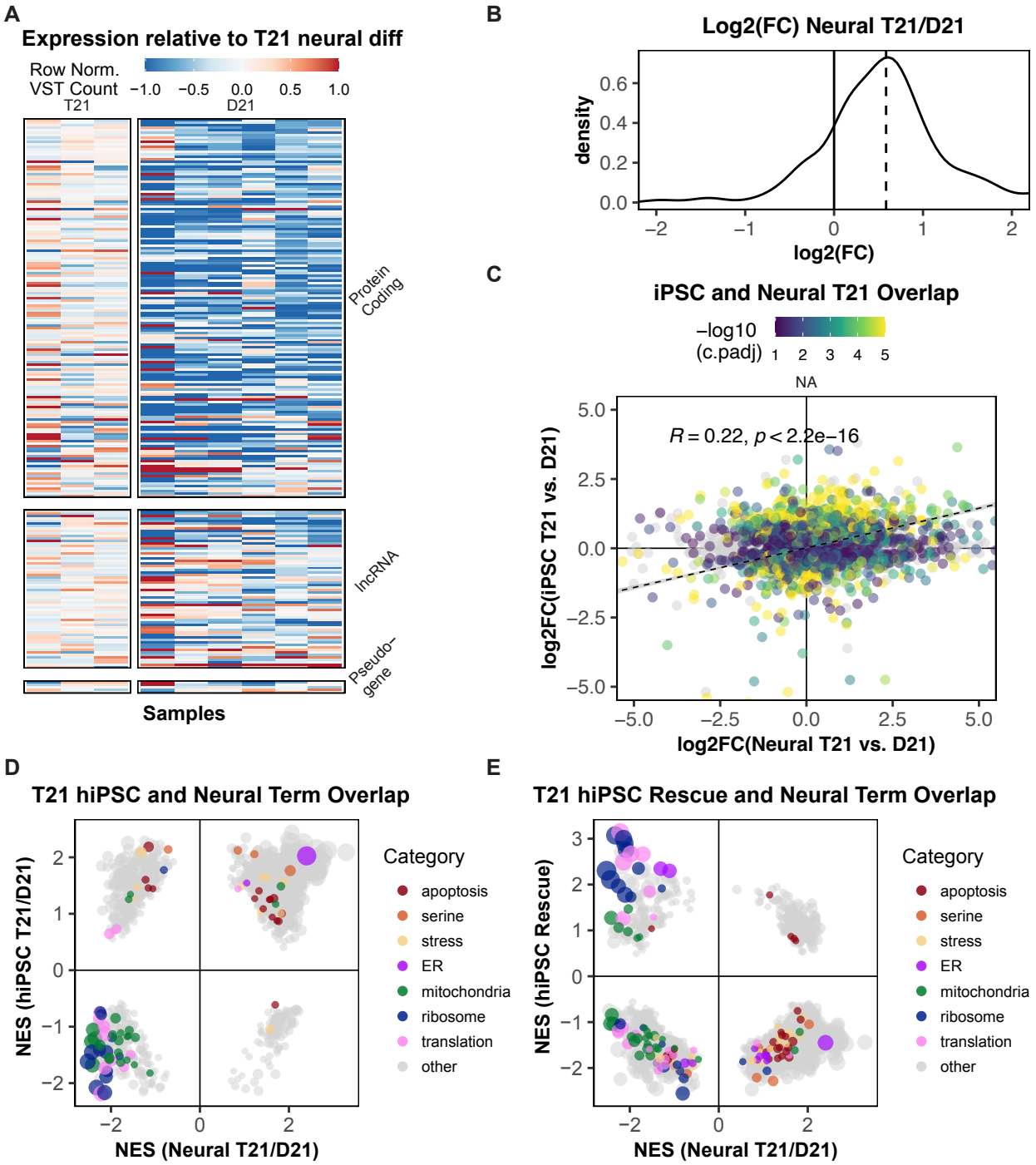
A
Expression relative to T21 neural diff
Row Norm.
VST Count
−1.0 −0.5 0.0 0.5 1.0
T21
D21
Protein Coding
lncRNA
Pseudo-gene
Samples
B
Log2(FC) Neural T21/D21
density
log2(FC)
C
iPSC and Neural T21 Overlap
−log10 (c.padj)
1 2 3 4 5
NA
R = 0.22, p < 2.2e−16
log2FC(iPSC T21 vs. D21)
log2FC(Neural T21 vs. D21)
D
T21 hiPSC and Neural Term Overlap
NES (hiPSC T21/D21)
NES (Neural T21/D21)
Category
apoptosis
serine
stress
ER
mitochondria
ribosome
translation
other
E
T21 hiPSC Rescue and Neural Term Overlap
NES (hiPSC Rescue)
NES (Neural T21/D21)
Category
apoptosis
serine
stress
ER
mitochondria
ribosome
translation
other

Figure 5

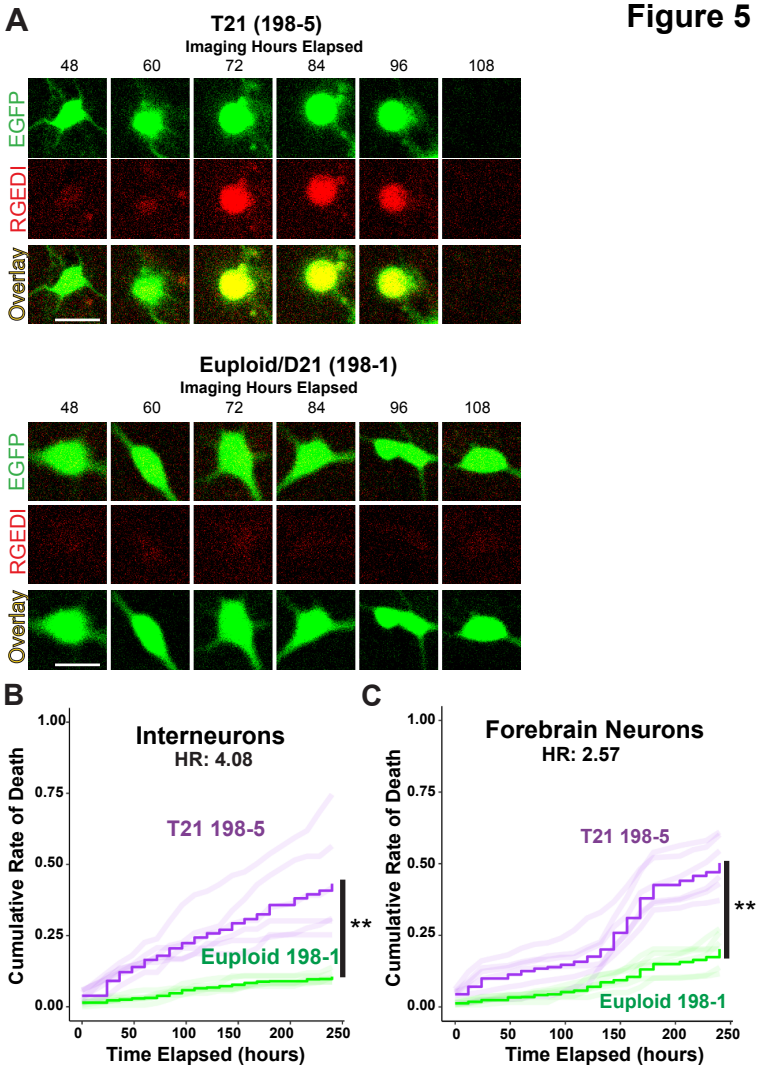
A
T21 (198-5)
Imaging Hours Elapsed
48
60
72
84
96
108
EGFP
RGEDI
Overlay
Euploid/D21 (198-1)
Imaging Hours Elapsed
48
60
72
84
96
108
EGFP
RGEDI
Overlay
B
Interneurons
HR: 4.08
T21 198-5
Euploid 198-1
**
Cumulative Rate of Death
1.00
0.75
0.50
0.25
0.00
0
50
100
150
200
250
Time Elapsed (hours)
C
Forebrain Neurons
HR: 2.57
T21 198-5
Euploid 198-1
**
Cumulative Rate of Death
1.00
0.75
0.50
0.25
0.00
0
50
100
150
200
250
Time Elapsed (hours)

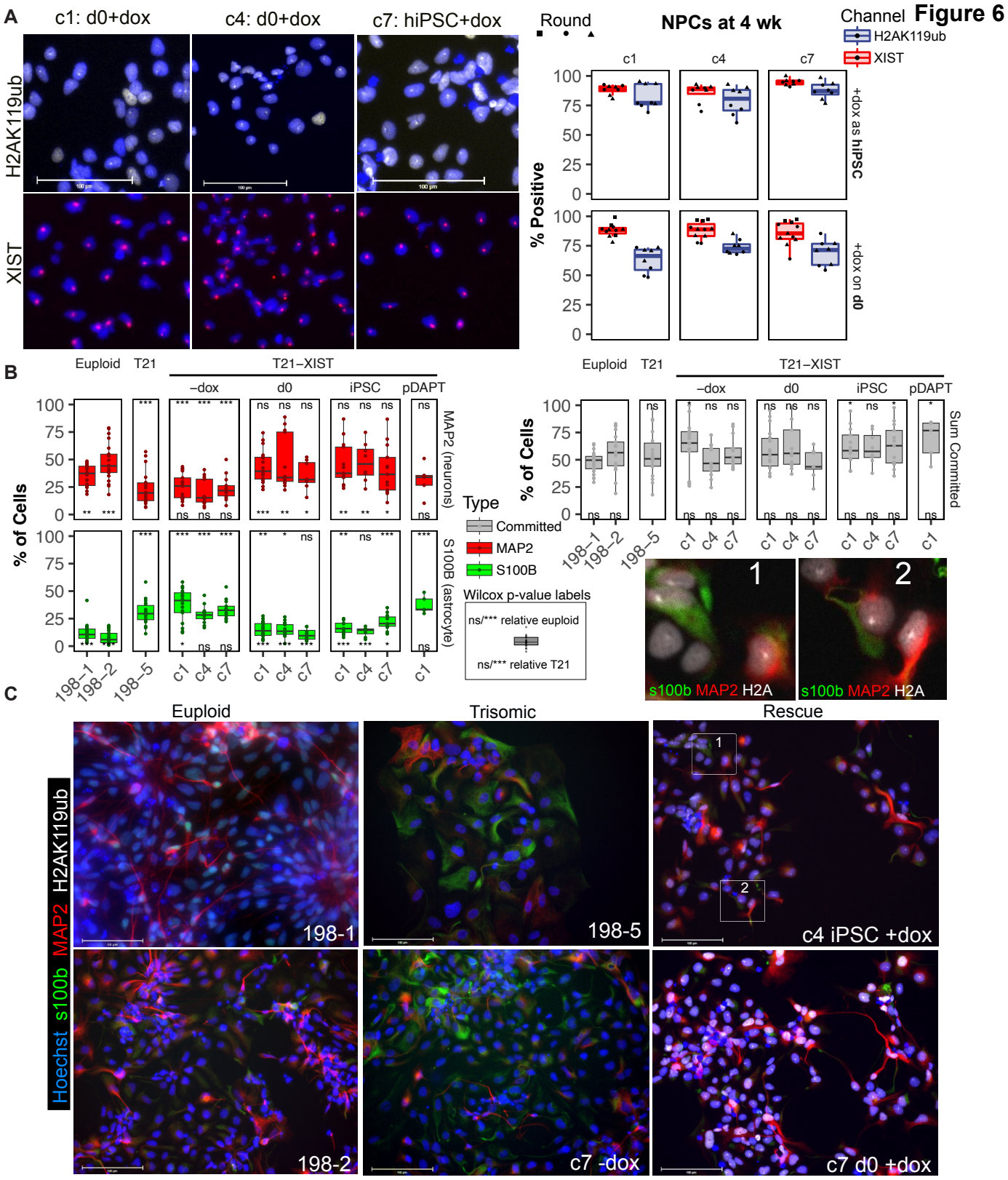
Figure 6
A
c1: d0+dox
c4: d0+dox
c7: hiPSC+dox
H2AK119ub
XIST
Round
NPCs at 4 wk
Channel
H2AK119ub
XIST
c1
c4
c7
% Positive
+dox as hiPSC
+dox on d0
B
Euploid
T21
T21−XIST
−dox
d0
iPSC
pDAPT
% of Cells
MAP2 (neurons)
S100B (astrocyte)
Sum Committed
198−1
198−2
198−5
Type
Committed
MAP2
S100B
Wilcox p-value labels
ns/*** relative euploid
ns/*** relative T21
s100b MAP2 H2A
C
Euploid
Trisomic
Rescue
H2AK119ub
MAP2
s100b
Hoechst
198-1
198-5
c4 iPSC +dox
198-2
c7 -dox
c7 d0 +dox

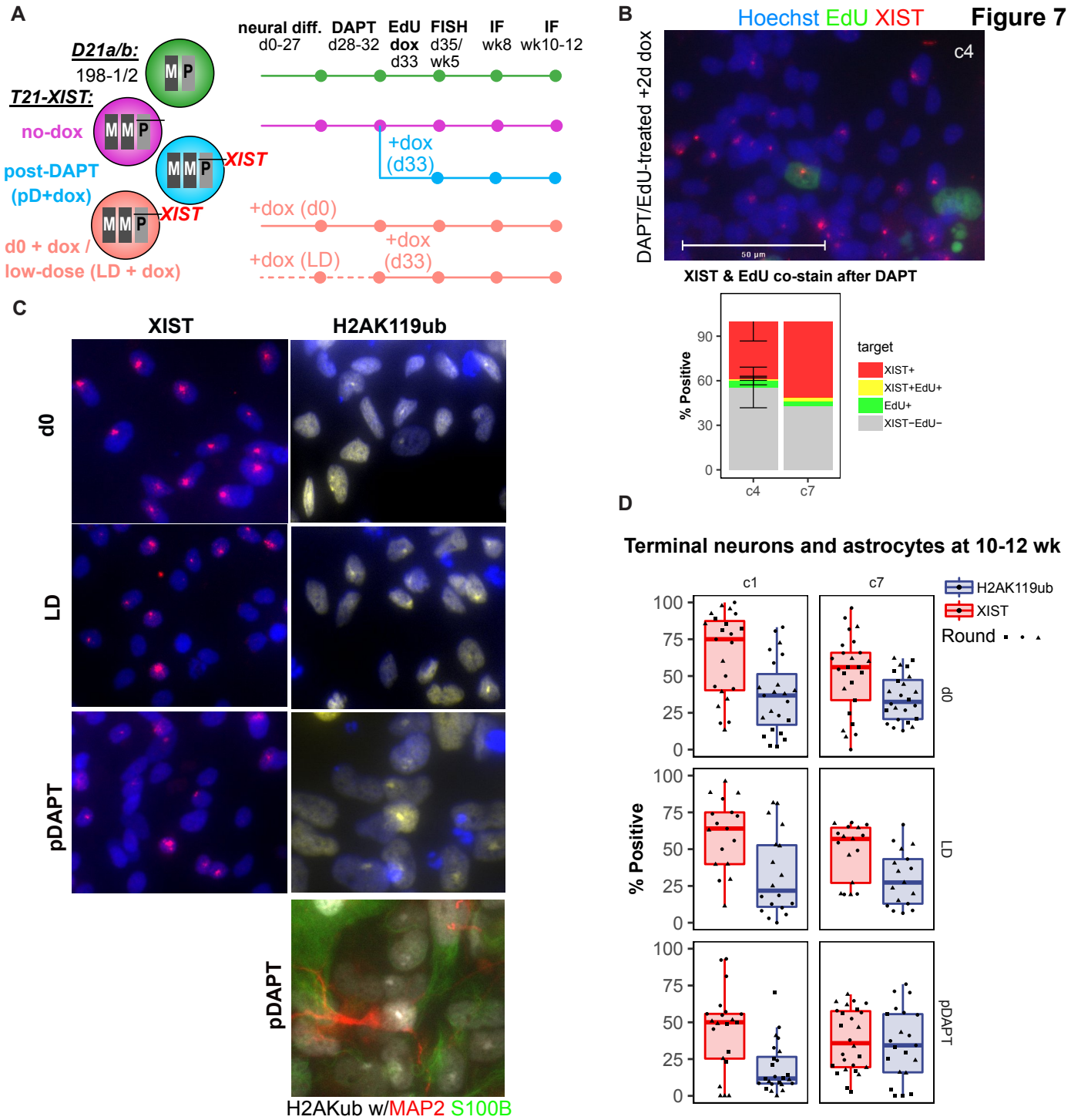
A
D21a/b:
198-1/2
T21-XIST:
no-dox
post-DAPT
(pD+dox)
d0 + dox /
low-dose (LD + dox)
XIST
XIST
neural diff.
d0-27
DAPT
d28-32
EdU
dox
d33
FISH
d35/
wk5
IF
wk8
IF
wk10-12
+dox
(d33)
+dox (d0)
+dox (LD)
+dox
(d33)
B
Hoechst EdU XIST
Figure 7
DAPT/EdU-treated +2d dox
c4
50 µm
XIST & EdU co-stain after DAPT
% Positive
target
XIST+
XIST+EdU+
EdU+
XIST−EdU−
c4
c7
C
XIST
H2AK119ub
d0
LD
pDAPT
pDAPT
H2AKub w/MAP2 S100B
D
Terminal neurons and astrocytes at 10-12 wk
c1
c7
H2AK119ub
XIST
Round
% Positive
d0
LD
pDAPT

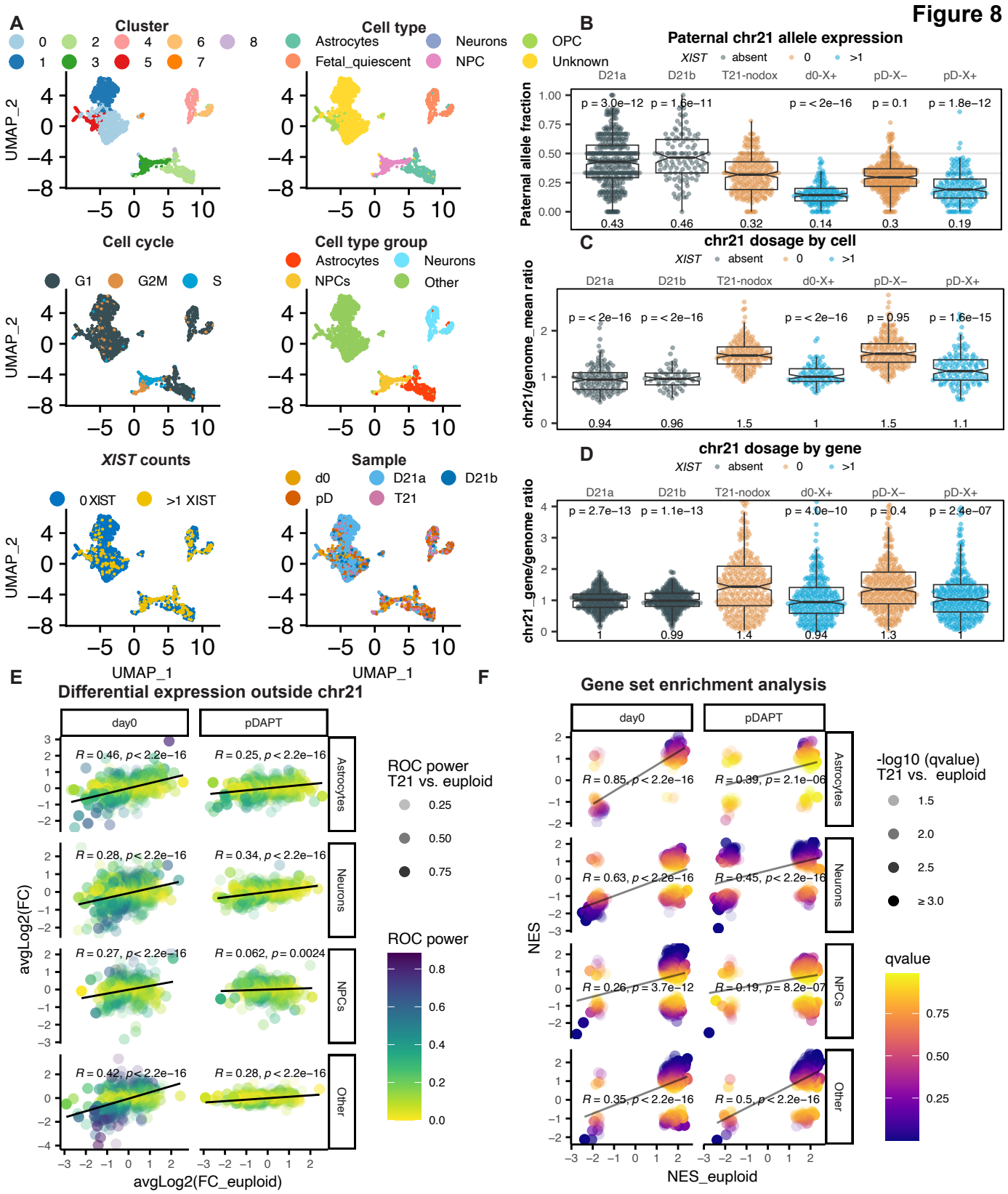
Figure 8
A
Cluster
Cell type
Astrocytes
Fetal_quiescent
Neurons
NPC
OPC
Unknown
Cell cycle
G1
G2M
S
Cell type group
Astrocytes
NPCs
Neurons
Other
XIST counts
0 XIST
>1 XIST
Sample
d0
pD
D21a
T21
D21b
UMAP_1
UMAP_2
B
Paternal chr21 allele expression
XIST absent 0 >1
D21a D21b T21-nodox d0-X+ pD-X− pD-X+
Paternal allele fraction
p = 3.0e−12 p = 1.6e−11 p = < 2e−16 p = 0.1 p = 1.8e−12
0.43 0.46 0.32 0.14 0.3 0.19
C
chr21 dosage by cell
chr21/genome_mean ratio
p = < 2e−16 p = < 2e−16 p = < 2e−16 p = 0.95 p = 1.6e−15
0.94 0.96 1.5 1 1.5 1.1
D
chr21 dosage by gene
chr21_gene/genome ratio
p = 2.7e−13 p = 1.1e−13 p = 4.0e−10 p = 0.4 p = 2.4e−07
1 0.99 1.4 0.94 1.3 1
E
Differential expression outside chr21
day0
pDAPT
Astrocytes
Neurons
NPCs
Other
R = 0.46, p < 2.2e−16
R = 0.25, p < 2.2e−16
R = 0.28, p < 2.2e−16
R = 0.34, p < 2.2e−16
R = 0.27, p < 2.2e−16
R = 0.062, p = 0.0024
R = 0.42, p < 2.2e−16
R = 0.28, p < 2.2e−16
avgLog2(FC)
avgLog2(FC_euploid)
ROC power
T21 vs. euploid
0.25
0.50
0.75
ROC power
0.8
0.6
0.4
0.2
0.0
F
Gene set enrichment analysis
R = 0.85, p < 2.2e−16
R = 0.39, p = 2.1e−06
R = 0.63, p < 2.2e−16
R = 0.45, p < 2.2e−16
R = 0.26, p = 3.7e−12
R = 0.19, p = 8.2e−07
R = 0.35, p < 2.2e−16
R = 0.5, p < 2.2e−16
NES
NES_euploid
-log10 (qvalue)
T21 vs. euploid
1.5
2.0
2.5
≥ 3.0
qvalue
0.75
0.50
0.25